1.59
X-ray Absorption Spectroscopy

CCC01063.0005

J. E. PENNER-HAHN
The University of Michigan, Ann Arbor, MI, USA

1.59.1 PHYSICS OF X-RAY ABSORPTION

CCC01063.0010

X rays are ionizing radiation and thus, by definition, have sufficient energy to eject a core election from an atom. Each core shell has a distinct binding energy, and thus if one plots X-ray absorption as a function of energy, the spectrum for any atom resembles the X-ray absorption spectrum for Pb, shown in Figure 1.[1–4] When the X-ray energy is scanned through the binding energy of a core shell, there is an abrupt increase in absorption cross-section. This gives rise to a

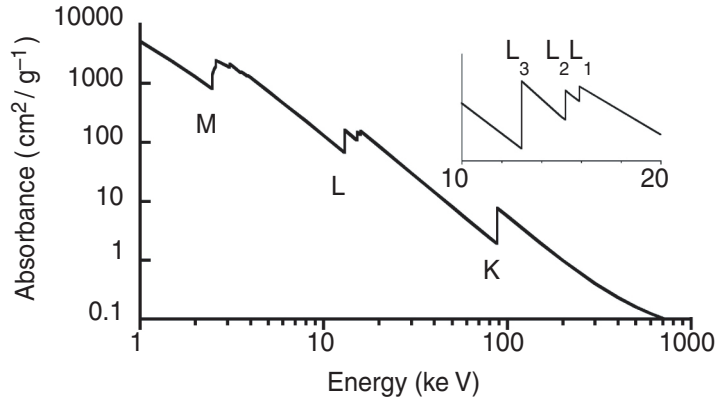

Figure 1 Low-resolution X-ray absorption spectrum for Pb. Three major transitions are seen (K, L, and M edges), corresponding to excitation of an electron from $n=1$, 2, and 3 shells, respectively. At higher resolution (inset) both the L and the M edges are split (see text for details).

so-called absorption edge, with each edge representing a different core–electron binding energy. The edges are named according to the principle quantum number of the electron that is excited: K for $n=1$, L for $n=2$, M for $n=3$, etc. The core–electron binding energy increases with increasing atomic number, ranging from 284 eV for the C K edge to 115,606 eV for the U K edge, with the L edges at significantly lower energies than the corresponding K edge (e.g., 270 eV for the Cl L_1 edge, 20,948 eV and 17,166 eV for the U L_2 and L_3 edges).

CCC01063.0015 Closer examination of Figure 1 (see inset) shows that the L edge is in fact three distinct L edges, named L_1, L_2, and L_3 in order of decreasing energy. L_1 corresponds to excitation of a $2s$ electron. The $2p$ excitation is split into two edges, L_2 and L_3, as a consequence of the spin–orbit coupling energy of the $2p^5$ configuration that is created when a $2p$ electron is excited. The higher energy of the $2p^5$ excited states is the $^2P_{1/2}$ term; This gives rise to the L_2 edge. At lower energy is the L_3 edge, corresponding to the $^2P_{3/2}$ excited state. Due to degeneracy, the L_3 edge has twice the edge jump of the L_2 and L_1 edges. In contrast with valence electron shells where spin–orbit coupling energies are relatively small, the spin–orbit coupling for core shells can be quite large. For Pb, the L_2-L_3 splitting is 2,165 eV ($1\,eV = 8{,}066\,cm^{-1}$). Analogous, albeit smaller, splitting occurs for the lower-energy edges, with 5 M edges, 7 N edges, etc. X-ray absorption spectroscopy (XAS) refers to the measurement of X-ray absorption cross-section in the vicinity of one or more absorbing edges.

1.59.1.1 X-ray Absorption Edges

CCC01063.0020 An absorption edge by itself is of little value beyond elemental identification.[5,6] However, if one examines any of the edges in Figure 1 in more detail, they are found to contain a wealth of information. This is illustrated by the schematic absorption edge shown in Figure 2. The absorption edge is not simply a discontinuous increase in absorption, as suggested by Figure 1, but in

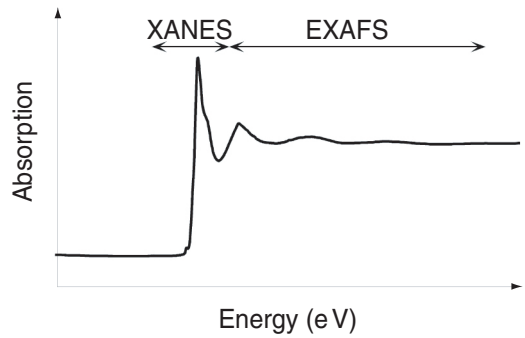

Figure 2 Schematic illustration of an X-ray absorption spectrum, showing the structured absorption that is seen both within ca. 50 eV of the edge (the XANES) and for several hundred to >1,000 eV above the edge (the EXAFS).

fact shows significant structure both in the immediate vicinity of the edge jump and well above the edge. The structure in the vicinity of the edge is sometimes referred to as X-ray absorption near-edge structure (XANES). The oscillations above the edge, which can extend for 1,000 eV or more, are often referred to as extended X-ray absorption fine structure (EXAFS). The distinction between XANES and EXAFS is arbitrary, since the same fundamental physical principles govern photoabsorption over the entire XAS region and there is no unambiguous definition that distinguishes between "near-edge" and "extended" structure. In an attempt to emphasize the essential similarity of these regions, the term XAFS (X-ray absorption fine structure) has gained some currency as a reference to the entire structured absorption region. Nevertheless, the terms EXAFS and XANES remain the most widely used, with some justification, since the XANES and EXAFS regions are generally analyzed differently. As described in detail below, the XANES region is sensitive to oxidation state and geometry, but is not, in most cases, analyzed quantitatively. The EXAFS region is sensitive to the radial distribution of electron density around the absorbing atom and is used for quantitative determination of bond length and coordination number. A fourth acronym, which is popular in the soft X-ray and surface science communities, is NEXAFS, standing for near-edge X-ray absorption fine structure. This acronym is redundant, since NEXAFS and XANES are used to refer to the same features, and is potentially confusing, given its similarity to EXAFS.

1.59.1.2 X-ray Fluorescence

CCC01063.0025 Absorption of an ionizing X-ray results in photoelectron ejection, leaving behind a highly excited core-hole state. This can relax by a variety of mechanisms, with the two most important being emission of an Auger electron and X-ray fluorescence. For lower-energy excitation, Auger emission can be the dominant relaxation process. For higher-energy excitation (e.g., for the K edges of elements with atomic numbers greater than 40), X-ray fluorescence is the primary relaxation process, with X-ray fluorescence yields approaching 1. For light elements, the X-ray fluorescence spectrum is quite simple. However, for heavy elements, a large number of X-ray emission lines are observed. The nomenclature associated with X-ray fluorescence lines predates a modern, quantum understanding of the origins of X-ray fluorescence and consequently there is not a simple relationship between the names of different emission lines and the origin of the line.[7] Some of the possible emission lines[7–9] are shown in Figure 3. Like all emission spectroscopy, X-ray fluorescence is governed by a series of selection rules. Consequently, only certain transitions, referred to as "diagram lines," are allowed. As with other spectroscopies, a variety of forbidden transitions (non-diagram lines) are also observed, and can yield important information (see discussion of high-resolution X-ray fluorescence, Section 1.59.4.2). Each element has unique "characteristic" X-ray emission energies which are, in most cases, well resolved from neighboring emission lines.[4,10,11]

1.59.1.3 Measurement of X-ray Absorption Spectra

CCC01063.0030 In the simplest case, measurement of an X-ray absorption spectrum involves only measurement of the incident and the transmitted X-ray flux. This can be accomplished, for example, with an

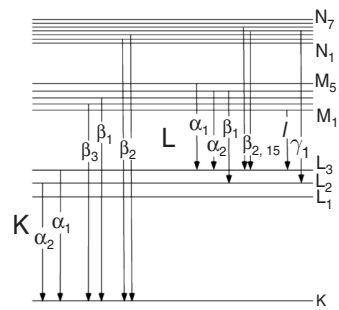

Figure 3 Nomenclature for selected X-ray emission lines. Excitation of a K shell results in K_α and K_β emission lines (originating from $n = 2$ and $n = 3$, respectively). At higher resolution, these can be resolved into $K\alpha_1$, $K\alpha_2$, with the splitting due to spin–orbit coupling. A similar pattern,with much greater complexity, is seen for L edge excitation. Redrawn from data in.[9] For a more complete list of emission lines, see.[7]

ionization chamber[12] in front of and behind the sample, using Beer's law to convert to absorption coefficient. This approach is limited to moderately concentrated samples (greater than ca. 10 mM or 500 ppm) and, depending on the energy of the absorption edge, even these concentrations may not be accessible. For example, sulfur or chlorine containing solvents are nearly opaque to lower-energy X rays and thus interfere with XAS measurements.

CCC01063.0035 To avoid the limitations of absorption, XAS spectra are frequently measured as fluorescence excitation spectra.[13] This is particularly important for dilute samples such as catalysts, biological samples, or environmental samples. The basic experimental geometry is illustrated in Figure 4. Providing the sample is dilute (absorbance due to the element of interest is much smaller than the background absorbance) or thin (total absorbance $<<1$), the intensity of the fluorescence X rays is proportional to the X-ray absorption cross-section (see Figure 4).[14] In most cases, the sample will emit a variety of X rays, both the fluorescence X rays of interest and a background of scattered X rays. In order to have good sensitivity, the fluorescence detector needs some kind of energy resolution to distinguish between the signal and background X rays. In some cases, energy resolution can be provided by a simple low-pass filter[15,16] although for the ultimate sensitivity it is necessary to use higher resolution in order to more effectively exclude background radiation. This is typically an energy-resolving solid-state fluorescence detector,[17–19] although recent advances with wavelength-resolving detectors (i.e., multilayer diffraction gratings) may be important in special cases.[20,21]

CCC01063.0040 In principle, any physical property that changes in proportion to X-ray absorption could be used to measure XAS spectra. In addition to X-ray fluorescence, properties that have been used include photoconductivity,[22] optical luminescence,[22–24] and electron yield, [25,26] although only the latter is widely used. Electron yield detection of XAS is particularly important for studies of surfaces. Since the penetration depth of an electron through matter is quite small, electron yield can be used to make XAS measurements surface sensitive. [27,28]

CCC01063.0045 Although XAS can be studied for virtually any X-ray absorption edge, experiments are simplest when they can be performed at atmospheric pressure. This limits the accessible X-ray energies to those greater than approximately 5 keV (for air) or 2 keV (for a He atmosphere). Lower energy measurements (i.e., measurements of the K edges for elements lighter than phosphorus) require that the sample be in vacuum in order to avoid excessive attenuation of the incident X-ray beam. Similarly, it is difficult, although not impossible, to make XAS measurements at energies above approximately 30 keV (K edge energy for Sn = 30.5 keV). However, this does not limit XAS significantly, since elements that are heavy enough to have K edge energies >30 keV have readily accessible L edge energies (the L_3 edge for Sn is at 4 keV). This means that XAS spectra can be measured for virtually every element, although measurements for elements lighter than phosphorus generally require that the sample be made vacuum compatible. X-ray absorption spectra can be measured for solids, liquids, or gases and do not require that samples have long-range order (i.e., be crystalline) or that samples possess particular magnetic properties (e.g., non-zero electron spin or specific isotopes). Measurements can be made at low temperature for studies of unstable samples, or at high temperature and/or pressure, for example for studies of catalysts under reaction conditions or of geochemical samples under conditions that approximate the inner mantle. This flexibility, combined with near universality, has made XAS a widely utilized technique in all areas of coordination chemistry.

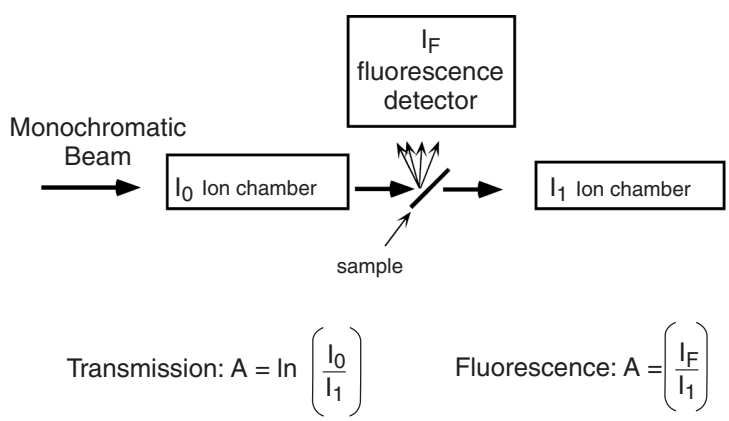

Figure 4 Typical experimental apparatus for XAS measurements. Incident and transmitted intensities are typically measured using an ion chamber; a variety of detectors can be used to measure X-ray fluorescence intensity for dilute samples (see text).

CCC01063.0050 The critical experimental detail that limits the utility of XAS, and that accounts for XAS having been an obscure technique prior to about 1975, is the need for an intense, tunable X-ray source. Conventional X-ray sources work much the same as the X-ray tube that was invented by Röntgen:[29] an electron beam strikes a target which emits both "characteristic" radiation (X-ray fluorescence lines) and a broad continuous background of bremsstrahlung radiation. Only the latter is useful for XAS, since XAS measurements require a broad band of X-ray energies. The intensity of monochromatic radiation that can be obtained from the bremsstrahlung radiation is too low for most XAS measurements.

CCC01063.0055 The development that allowed XAS to become a routine analytical tool was the recognition that the electron storage rings that are used in high-energy physics can serve as an extremely intense X-ray source. When an electron beam is accelerated, for example by using a magnetic field to cause the beam to follow the curvature of a storage ring, the electron beam radiates a broad spectrum of "synchrotron" radiation. From modest beginnings in the early 1970s, synchrotron radiation laboratories have grown enormously to the point that there are now over 75 laboratories, either planned, under construction, or in operation, devoted to the production of synchrotron radiation in one form or another, located in 23 countries.[30] A selection of some of the more important sources for XAS is given in Table 1. Other countries that will soon join this list include Armenia, Canada, Jordan, Spain, Thailand, and the Ukraine. Each of these laboratories is based around an electron (or positron) storage ring. Ring sizes vary, but modern synchrotrons typically have a circumference of approximately one kilometer. This size is large enough to accommodate anywhere from 10 to perhaps 100 independent "beamlines" (the hardware that transports the X rays from the synchrotron source to the experimental apparatus) at each synchrotron laboratory.

CCC01063.0060 The importance of synchrotron radiation can be seen by comparing the X-ray flux that is available from X-ray tubes with that available from synchrotron sources (Figure 5). The spectral brightness (X-ray flux normalized by area that is irradiated and divergence of the beam) of the most powerful sources is more than 10 orders of magnitude greater than that available from X-ray tubes. Another advantage of synchrotron sources is that the synchrotron X-ray beam is polarized, thus permitting orientation-dependent measurements for ordered samples. In addition,

Table 1 Major synchrotron sources for XAS.

Country	*Location*	*Synchrotron source*
Brazil	Campinas	LNLS
China (PRC)	Beijing	BSRF
	Hefei	NSRL
China (ROC-Taiwan)	Hsinchu	SRRC
Denmark	Aarhus	ASTRID
France	Grenoble	ESRF
	Orsay	LURE
Germany	Berlin	BESSY
	Hamburg	HASYLAB/DESY
India	Indore	INDUS
Italy	Trieste	ELETTRA
Japan	Nishi Harima	Spring-8
	Tsukuba	Photon Factory
Korea	Pohang	Pohang Light Source
Russia	Moscow	Siberia 1
	Novosibirsk	VEPP
Singapore	Singapore	SSLS
Sweden	Lund	MAX
Switzerland	Villigen	SLS
UK	Daresbury	SRS
USA	Argonne, IL	APS
	Baton Rouge, LA	CAMD
	Berkeley, CA	ALS
	Ithaca, NY	CHESS
	Stanford, CA	SSRL
	Stoughton, WI	Aladdin
	Upton, NY	NSLS

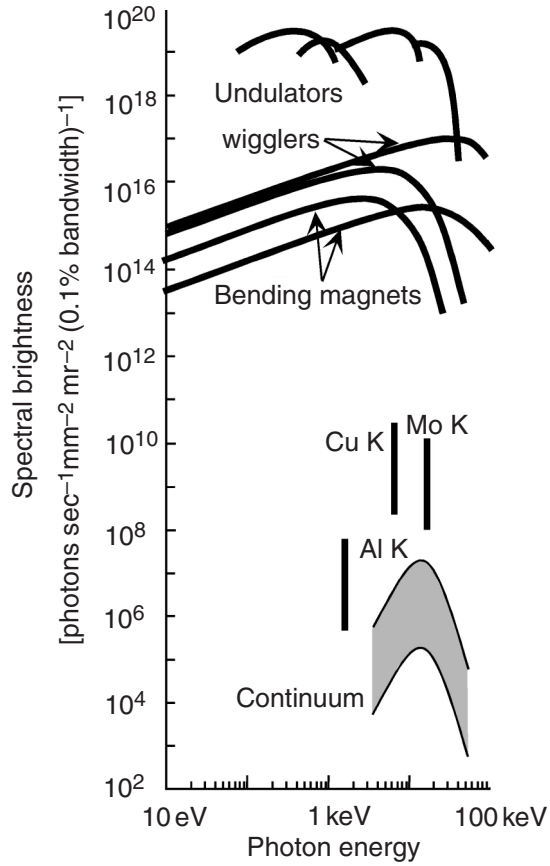

Figure 5 Typical spectral brightness of different X-ray sources (details will vary depending on the properties of the source). X-ray tube spectra, shown in gray (bremsstrahlung) and vertical bars (characteristic lines), can vary by two orders of magnitude depending on whether fixed or rotating anodes are used. Synchrotron sources vary depending on the details of the storage ring and on the energy of the electron beam. Representative data are shown for electron beam energies of 2 GeV and 7 GeV. In addition to the bending magnets, which cause the electron beam to curve around the storage ring, more recent synchrotrons use "insertion devices" to alter the orbit of the electron beam. These can produce broad-band spectra ("wigglers") or relatively narrow spectra ("undulators") depending on the details of the insertion device design. Redrawn from data in.[9]

with appropriate design, beamline can be made to produce circularly polarized X rays, thus permitting magnetic circular dichroism studies in the X-ray region.

CCC01063.0065 This increase in X-ray intensity, together with the development of synchrotron laboratories with facilities dedicated to measurement of XAS, has allowed XAS to develop into a relatively routine analytical tool. It is straightforward to measure XAS spectra for transition metal solutions with concentrations greater than 1 mM (ca. 50 ppm) and it is possible, using the most intense synchrotron sources and the most sensitive detectors, to measure high-quality XAS spectra for samples containing less than 1 ng of the metal of interest. Typical sample volumes range from one mL to one μL and with microfocused X-ray beams (see below) even smaller volumes can be studied.

1.59.2 EXTENDED X-RAY ABSORPTION FINE STRUCTURE

1.59.2.1 Theoretical Description of EXAFS Spectra

1.59.2.1.1 Single scattering

CCC01063.0070 The EXAFS region is typically taken as starting 20–30 eV above the edge jump. At these energies, the X-ray excited photoelectron has significant energy, and thus has a de Broglie wavelength that

is comparable to the interatomic distances. The EXAFS photoexcitation cross-section is modulated by the interference between the outgoing and the back-scattered photoelectron waves as illustrated schematically in Figure 6. At energy E_1, the outgoing and the back-scattered X rays are in phase, resulting in constructive interference and a local maximum in the X-ray photoabsorption cross section. At higher X-ray energy, the photoelectron has greater kinetic energy and thus a shorter wavelength, resulting in destructive interference and a local minimum in photoabsorption cross section (energy E_2). The physical origin of EXAFS is thus electron scattering, and EXAFS can be thought of as a spectroscopically detected scattering method, rather than as a more conventional spectroscopy.

CCC01063.0075 For a single absorber–scatterer pair (for example, in a diatomic gas) this alternating interference will give rise to sinusoidal oscillations in the absorption coefficient if the energy is given in units proportional to the inverse photoelectron wavelength (the photoelectron wavevector, or k, defined as in Equation (1)). In Equation (1), the threshold energy, E_0, is the binding energy of the photoelectron.

$$k = \sqrt{2m_e(E - E_0)/h^2} \tag{1}$$

CCC01063.0080 In XAS analyses, it is typical to define the EXAFS, $\chi(k)$, as the fractional modulation in the X-ray absorption coefficient as in Equation (2), where μ is the observed absorption coefficient and μ_0 is the absorption that would be observed in the absence of EXAFS effects. Since μ_0 cannot be directly measured, it is approximated, typically by fitting a smooth spline function through the data. Division by μ_0 normalizes the EXAFS oscillations "per atom," and thus the EXAFS represents the average structure around the absorbing atoms.

$$\chi(k) = \frac{\mu - \mu_0}{\mu_0} \tag{2}$$

CCC01063.0085 When plotted as $\chi(k)$, EXAFS oscillations have an appearance similar to that shown in Figure 7. The amplitude of the EXAFS oscillations is proportional to the number of scattering atoms, the frequency of the oscillations is inversely proportional to the absorber–scatterer distance, and the shape of the oscillations is determined by the energy dependence of the photoelectron scattering, which depends on the identity of the scattering atom. For quantitative analyses, the EXAFS can be described[31–33] by an equation such as Equation (3), with the summation taken over all of the scattering atoms near the absorber.

$$\chi(k) = \sum_s \frac{N_s A_s(k) S_0^2}{k R_{as}^2} \exp(-2R_{as}/\lambda(k)) \exp(-2k^2\sigma_{as}^2) \cdot \sin(2kR_{as} + \phi_{as}(k)) \tag{3}$$

CCC01063.0090 In Equation (3), the parameters that are of principal interest for coordination chemistry are the number of scattering atoms, N_s and the absorber–scatterer distance, R_{as}. However, there are a variety of other parameters that must either be determined or be defined in order to extract the chemically relevant information. Chief among these are $A_s(k)$ and $\phi_{as}(k)$. These represent, respectively, the energy dependence of the photoelectron scattering, and the phase shift that the photoelectron wave undergoes when passing through the potential of the absorbing and scattering atoms. These amplitude and phase parameters contain the information necessary to identify the scattering atom. Thus, for example, sulfur and oxygen introduce phase shifts, $\phi_{as}(k)$, that differ by approximately π. Unfortunately, both $A_s(k)$ and $\phi_{as}(k)$ depend only weakly on scatterer identity, and thus it is difficult to identify the scatterer with precision. This means that O and N, or S and Cl, typically cannot be distinguished, while O and S can.

CCC01063.0095 The EXAFS amplitude falls off as $1/R^2$. This reflects the decrease in photoelectron amplitude per unit area as one moves further from the photoelectron source (i.e., from the absorbing atom). The main consequence of this damping is that the EXAFS information is limited to atoms in the near vicinity of the absorber. There are three additional damping terms in Equation (2). The S_0^2 term is introduced to allow for inelastic loss processes and is typically not refined in EXAFS analyses. The first exponential term is a damping factor that arises from the mean free path of the photoelectron ($\lambda(k)$). This serves to limit further the distance range that can be sampled by EXAFS. The second exponential term is the so-called "Debye–Waller" factor. This damping reflects the fact that if there is more than one absorber–scatterer distance, each distance will contribute EXAFS oscillations of a

slightly different frequency. The destructive interference between these different frequencies leads to damping in the EXAFS amplitude. The Debye–Waller factor, σ_{as}, is the root-mean-square deviation in absorber–scatterer distance. This damping is always present due to zero-point thermal motion, and may, for polyatomic systems, also occur as a consequence of structural disorder. As a consequence of the damping terms in Equation (3), EXAFS oscillations are typically only observed for atoms within approximately 5 Å of the absorbing atom.

CCC01063.0100 In Equation (3) the backscattering amplitude and phase are assumed to depend only on the identity of the absorber and the scatterer. This derives from the so-called plane wave approximation, in which the curvature in the photoelectron wave is neglected and the photoelectron is treated as a plane wave.[34–36] For energies well above the X-ray edge (high k, short photoelectron wavelength) or for long absorber–scatterer distances this is a fairly reasonable assumption. It is not, however, a good assumption for most of the useful EXAFS region. Modern approaches to calculating amplitude and phase parameters (see Section 1.59.2.2) include spherical wave corrections to the amplitude and phase, thus introducing a distance dependence to A_s and ϕ_{as}.

1.59.2.1.2 Multiple scattering

CCC01063.0105 The discussion above assumed that the X-ray excited photoelectron was scattered only by a single scattering atom before returning to the absorbing atom (e.g., Figure 6). In fact, the X-ray excited photoelectron can be scattered by two (or more) atoms prior to returning to the absorbing atom. Multiple scattering is particularly important at low k where the photoelectron has a very low energy and consequently a long mean-free path, allowing it to undergo extensive multiple scattering. Multiple scattering is particularly strong if the two scattering atoms are nearly collinear since the photoelectron is strongly scattered in the forward direction. In this case, the EXAFS oscillations due to the multiple scattering pathway (absorber → scatterer 1 → scatterer 2 → scatterer 1 → absorber in Figure 8) can be as much as an order of magnitude stronger than that due to the single scattering pathway (absorber → scatterer 2 → absorber).[37–39] Failure to account for multiple scattering can lead to serious errors in both EXAFS amplitude and phase, with consequent errors in the apparent coordination number and bond length.

CCC01063.0110 Multiple scattering is extremely angle dependent. For scattering angles less than ca. 150° (the angle A–S_1–S_2 in the example above), multiple scattering is weak and can often be neglected. However, for angles between 150° and 180°, multiple scattering must be considered. The angle dependence of multiple scattering means that EXAFS can, at least in principle, provide direct information about bond angles. Even when accurate angular information cannot be obtained (see below), multiple scattering is still important because it gives certain coordinating groups unique EXAFS signatures. These include both linear ligands such as CO and CN^-, as well as rigid cyclic ligands such as pyridine or imidazole. This can, in some cases, improve the limited sensitivity of EXAFS to scatterer identity. For example, in biological systems water and the imidazole group of

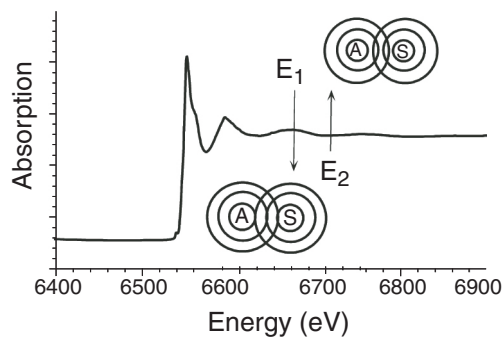

Figure 6 Schematic illustration of the physical basis of EXAFS oscillations. The X-ray excited photoelectron is represented by concentric circles around the absorbing atom (A), with the spacing between circles representing the de Broglie wavelength of the photoelectron. The photoelectron is scattered by surrounding atoms (indicated by a single atom S in the figure). At energy E_1, the out-going and back-scattered waves are in phase, resulting in constructive interference and a local maximum in photoabsorption cross-section. At a slightly higher energy E_2 (shorter photoelectron wavelength) the absorber–scatterer distance gives destructive interference and a local minimum in absorbance.

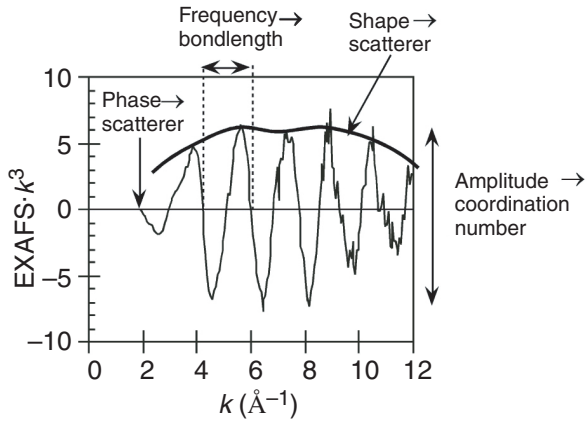

Figure 7 EXAFS spectrum calculated as in Equation (2). The structural information is encoded in the amplitude, the shape, the phase, and the frequency of the oscillations. Data have been multiplied by k^3 to enhance the oscillations at high k. These data (the Fe EXAFS for a di-μ-sulfido bridged Fe dimer) show a characteristic "beat" in amplitude at $k=7\,\text{Å}^{-1}$, due to the presence of both Fe—S and Fe—Fe scattering). Note the noise at high k. For dilute samples, noise often limits the data to $k=12\,\text{Å}^{-1}$ or less.

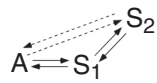

Figure 8 Illustration of single scattering (dashed line) and multiple scattering (solid lines) pathways. The absorbing atom is A, which is surrounded in this example by two scattering atoms, S_1 and S_2.

a histidine amino acid have nearest-neighbor EXAFS that is virtually indistinguishable (O vs. N). However, the imidazole group can be identified by its unique multiple-scattering signature.[37,40–42]

1.59.2.1.3 Other corrections to the EXAFS equation

CCC01063.0115 There are a variety of additional correction factors that are not included in Equation (3). These are not widely used and can often be ignored in data analysis. However, for the most accurate description of the EXAFS, it is necessary to include several other effects. The discussion thus far has assumed that there is only a single core electron that is excited by the incident X-ray. However, the incident X-ray has sufficient energy to eject more than one electron, and this can give rise to additional small edge jumps above the main edge due to the opening of absorption channels creating double-hole configurations such as [1*s*4*p*], [1*s*3*d*], and [1*s*3*p*].[43–45] Multielectron excitations will take place whenever the incident X-ray energy equals the sum of two core-electron excitations. In practice, multielectron excitations are most important near the edge and are often detectable only for samples that have very weak EXAFS signals (for example, for ionic solutions, which have only weak cation-solvent interactions).[46–48] A second complication is that the photoelectron wave can be scattered not only by atoms but also by the potential barrier that develops when a free atom is embedded into a condensed phase. In this case, the free-atom potential is modified and the resulting scattering of the outcoming photoelectron produces weak oscillations in the absorption cross section.[49,50] This can be treated as a variation in the atomic background,[51,52] and is sometimes referred to as "atomic" EXAFS. As with multielectron features, atomic EXAFS features are quite weak and are typically seen only near the absorption edge. Since this is a region that is very sensitive to background subtraction (the μ_0 in Equation (2)) it is not always clear what physical phenomenon is responsible for the observed spectral anomalies,[53] particularly in view of the similar appearance of multielectron excitations and atomic EXAFS.[54,55]

1.59.2.2 Programs for Calculating and Analyzing EXAFS

CCC01063.0120 The analysis of EXAFS data can be divided into two stages: reduction of the measured absorption spectra to EXAFS (i.e., application of Equation (2)) and analysis of the $\chi(k)$ data to obtain structural parameters (N_s, σ_{as}, and R_{as}). Data reduction involves both normalization (Equation

(2)) and conversion to k space (Equation (1)). Data analysis is, at least in principle, a relatively straightforward problem of optimizing the variable parameters in Equation (3) so as to give the best fit to the observed data using some sort of non-linear least-squares fitting procedure. Over 20 programs are available to accomplish the data reduction and analysis.[56] Most are quite similar in their functionality.

CCC01063.0125 In order to fit EXAFS data, it is first necessary to determine the parameters that define the scattering ($A_s(k)$, S_0^2, $\phi_{as}(k)$, and $\lambda(k)$). This can be done using *ab initio* calculations or from model compounds of known structure. In recent years, the available theoretical methods for quickly and accurately calculating these parameters have improved dramatically. *Ab initio* calculations are now relatively straightforward, with three main programs that are in wide use: FEFF[39,57,58], EXCURVE[41,59], and GNXAS[60–62]. Although these differ in the particulars of their approach to EXAFS, all give approximately the same structural parameters.[63] In contrast, older approaches, particularly those using the earliest plane-wave parameters[34–36] often fail to give accurate structural results. Despite these well-known errors,[64] publications using these parameters continue to appear occasionally in the literature. Regardless of what theoretical parameters are used, careful comparison with model compounds remains important for proper calibration of the calculated parameters.[65]

CCC01063.0130 Using carefully calibrated parameters to determine S_0^2 and E_0, it is possible to obtain excellent accuracy for EXAFS bond length determinations. Typical values, determined by measuring data for structurally defined complexes, are 0.01–0.02 Å for nearest-neighbor distances and somewhat worse for longer distance interactions. The precision of bond-length determinations is even better, with experimentally determined reproducibilities as good as 0.004 Å.[66] Coordination number is less well defined, due in part to correlation between N and σ^2 (see Equation (3)). In many cases, EXAFS coordination numbers cannot be determined to better than ±1. As noted above, EXAFS has only weak sensitivity to atomic type. Typically it is only possible to determine the atomic number of the scattering atom to ±10. Despite these limitations, the ability to provide structural information, particularly highly accurate bond lengths, for non-crystalline systems, has made EXAFS an extremely important tool in coordination chemistry.

1.59.2.2.1 Fourier transforms

CCC01063.0135 Although Equation (3) provides a complete description of the EXAFS oscillations, it is not a particularly convenient form for visualizing the information content of an EXAFS spectrum. As with NMR spectroscopy, Fourier transformation can be used to decompose a k-space signal into its different constituent frequencies.[67] This is illustrated using the EXAFS data[68] for a THF solution of CuCN·2LiCl. The EXAFS spectrum (Figure 9) clearly contains more than one frequency, based on the complex variation in amplitude. For EXAFS, the canonical variables are k (in Å^{-1}) and R (in Å), and the Fourier transform (FT) of an EXAFS spectrum gives a

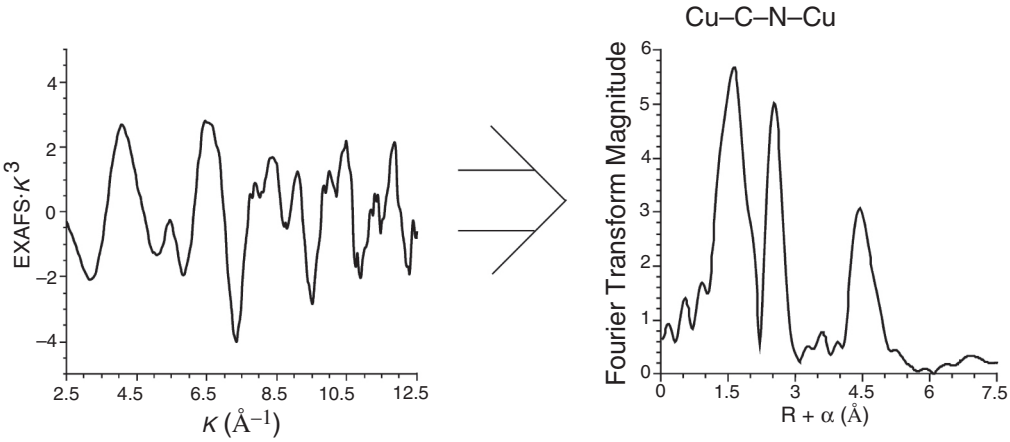

Figure 9 EXAFS data (left) and its Fourier transform (right) for a THF solution of CuCN·2LiCl.[68] The Fourier transform clearly shows three distinct peaks, reflecting the presence of three distinct absorber–scatterer interactions, as indicated above the Fourier transform.

pseudo-radial distribution function. The Fourier transform of the data in Figure 9 shows that there are three principal frequencies that contribute to this spectrum. These are due to scattering from the Cu nearest neighbors (C from the cyanide), the next-nearest neighbors (N from the cyanide), and the next-next-nearest neighbors (an additional Cu coordinated to the distal end of the cyanide). The third peak thus clearly shows formation of a $(CuCN)_n$ oligomer under these conditions. The FT amplitude is not a true radial distribution function since the amplitude cannot be related directly to electron density around the absorber due to the $A_s(k)$ factor and the damping factors in Equation (3), and the apparent distances in the FT are shifted by about -0.5 Å due to the phase shift $\phi_{as}(k)$. The unusually high intensity of the second and third peaks in Figure 9 is due to the near linearity of the Cu—C—N—Cu unit, which leads to intense multiple scattering.

CCC01063.0140 The FT is useful for obtaining a qualitative understanding of a system. However, Fourier transforms are subject to several potential artifacts and cannot be used for quantitative data analysis. Depending on the resolution of the data (see below), multiple shells of scatterers do not necessarily give rise to multiple peaks in the FT.[69] Perhaps more important, two peaks may appear to be well-resolved despite the fact that they have substantial overlap. This is illustrated in Figure 10, where the top FT is for the sum of two EXAFS spectra (simulated for Mn—O distances of 1.9 Å and 2.1 Å) while the bottom shows the FTs of the two individual components. Although the two peaks appear to be well resolved, each peak, in fact, contains significant contributions from the other scatterer. This phenomenon is due to the fact that the FT is a complex function, including both real and imaginary components. Typically (e.g., Figure 10) what is plotted is the modulus of the Fourier transform, thus losing all phase information. In Figure 10, the Fourier components from the two different scatterers interfere destructively, leading to the minimum in the modulus.

CCC01063.0145 Interference such as that in Figure 10 is particularly important if the data are Fourier filtered. Fourier filtering involves selecting certain frequencies in R space to use for a back Fourier transform (back into k space). Filtering can greatly simplify the curve-fitting problem, since the filtered data contains only a single shell of scatterers (this amounts to dropping the summation in Equation (3)). However, as illustrated by Figure 10, filtering can have unexpected consequences. Neither of the peaks in the top panel actually represents the scattering from a single atom, despite the apparent resolution of the data; attempts to fit these as though they represent single shells leads to erroneous conclusions.[69]

1.59.2.2.2 Curve fitting

CCC01063.0150 A typical coordination complex might have six different nearest-neighbor distances, together with a larger number of longer distance interactions. Although each of these contributes a slightly different signal to the overall EXAFS, it is not realistic to refine all of the different absorber–

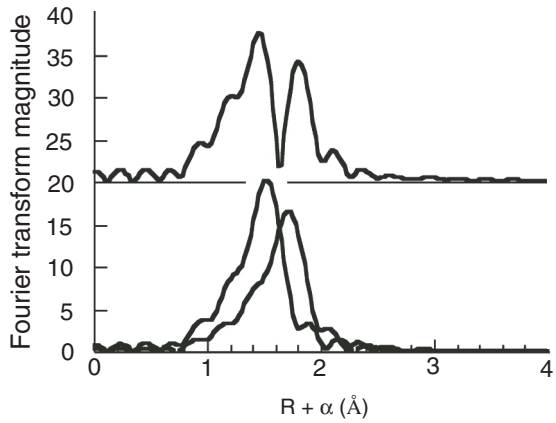

Figure 10 Fourier transform of the simulated EXAFS for two shells of scatterers. Data calculated for Mn—O distances of 1.9 and 2.1 Å. (top) FT of the sum of the EXAFS signals of each shell. (bottom) FTs of the two individual components. Although there is significant overlap in the two shells, the FT of the sum appears to show baseline separation as a consequence of phase differences in the Fourier terms.

scatterer interactions. Typically, absorber–scatterer interactions are grouped into "shells." A shell is a group of similar scatterers at approximately the same distance from the absorber. A non-linear least-squares fitting algorithm is then used to model the observed data using Equation (3). A frequent problem is to determine whether the inclusion of an additional shell (i.e., an additional sum in Equation (3)) is justified. Since data are available only over a finite k range and since there is always some noise, particularly at high k, it can be difficult to distinguish genuine improvements in the fit from the inevitable improvement that occurs when a least-squares fitting engine is provided with more variable parameters. One solution is to not use a simple mean-square deviation (Equation (4)) as the measure of fit quality, but to replace this with a reduced chi-squared statistic, ξ^2 (Equation (5)).[64]

$$F = \sqrt{\frac{\sum_{i=1}^{N}(\chi_{\text{obs}}(k_i) - \chi_{\text{calc}}(k_i))^2}{N}} \tag{4}$$

$$\frac{\xi^2 = (N_{\text{idp}}/\nu)\cdot\sum_{i=1}^{N}(\chi_{\text{obs}}(k_i) - \chi_{\text{calc}}(k_1))^2/\varepsilon_i^2}{N} \tag{5}$$

In Equation (5), ν is the number of degrees of freedom, calculated from Equation (6), where N_{idp} is the number of independent data points and N_{var} is the number of variables that are refined.

$$\nu = N_{\text{idp}} - N_{\text{var}} \tag{6}$$

The sum in Equation (5) is calculated over all of the measured data points, N, and the deviation at each point is weighted by $1/\varepsilon_i^2$, where ε_i is the root-mean-square uncertainty in χ_{obs}. The $1/\nu$ weighting introduces a penalty for adding additional, unnecessary, shells of scatterers.

CCC01063.0155 The number of independent data points in an EXAFS spectrum is not equal to the number of measured data points.[64,70] In most cases, EXAFS spectra are significantly oversampled, so that $N_{\text{idp}} << N$. The limitation in N_{idp} results from the fact that EXAFS spectra are "band-limited" and thus do not contain contributions from all possible frequencies. N_{idp} can be estimated as in Equation (7).

$$N_{\text{idp}} = \frac{2\Delta k \Delta R}{\pi} \tag{7}$$

Since k_{min} is approximately 2 Å, k_{max} is often 12–14 Å^{-1} or less, and the R range over which EXAFS signals are seen is approximately 1−4 Å, N_{idp} can be 20 or less, although larger values are possible. For filtered data, N_{idp} is often much smaller; For $\Delta R \leq 0.8$ Å, N_{idp} may be as small as 6–8. In such cases, it may be impossible to obtain meaningful fits using two shells of scatterers. If three parameters (R, σ^2, and N) are refined per shell, then for two shells there may be no free parameters. Although the fit may reproduce the data perfectly, the refined structural parameters need not be physically meaningful.[71]

CCC01063.0160 The number of degrees of freedom increases linearly with R, therefore if data can be detected to high R, for example by making measurements at very low temperatures, it should be possible to obtain sufficient data to permit a detailed description of the structure. Outer shell data is particularly interesting because it is sensitive to multiple scattering, and thus can provide information about the three-dimensional geometry of the complex. Unfortunately, the number of multiple-scattering atoms and the number of possible multiple-scattering paths (e.g., Figure 8), increases approximately as R^2. This makes it unlikely that EXAFS alone will ever be able to provide reliable structural information for atoms beyond the third, or perhaps the fourth coordination shell.[69,72]

1.59.2.3 Limitations of EXAFS

CCC01063.0165 The ability to determine accurate structures for non-crystalline samples has made EXAFS extremely useful in coordination chemistry. However, there are several practical limitations to

the ability of EXAFS to probe structure. One involves the ability of EXAFS to resolve contributions from two different scatterers. The best resolution that can be achieved[73] is given in Equation (8).

$$\Delta R \geq \pi/2\Delta k \tag{8}$$

This gives $\Delta R \geq 0.13$ Å for data to $k_{max}=12$ Å^{-1}. However, this estimate is generally too optimistic as illustrated by Figure 11, which shows pairs of simulated EXAFS spectra for one shell (dashed lines) and two shells (solid lines).[69] The top trace shows the simulation for a pair of scatterers separated by 0.25 Å (R_1=1.75, R_2=2.00 Å). There is an obvious "beat" in the EXAFS amplitude at $k \approx 8$ Å^{-1} which distinguishes these data from the EXAFS for a single shell at the same average distance (1.875 Å). The middle simulation shows that there is still a beat when ΔR decreases to 0.15 Å, although the beat has moved close to k_{max}. It is straightforward to distinguish between two shells and a single shell at the average distance (1.925 Å, dashed line). However, if the single-shell simulation is damped with an exponential damping factor (lower traces) it is now nearly impossible to distinguish between one shell (dashed line) and two shells (solid line). It is only at high k, where the noise in an experimental spectrum is the largest, that the one- and two-shell simulations are distinguishable. It is unlikely that these spectra could be distinguished for

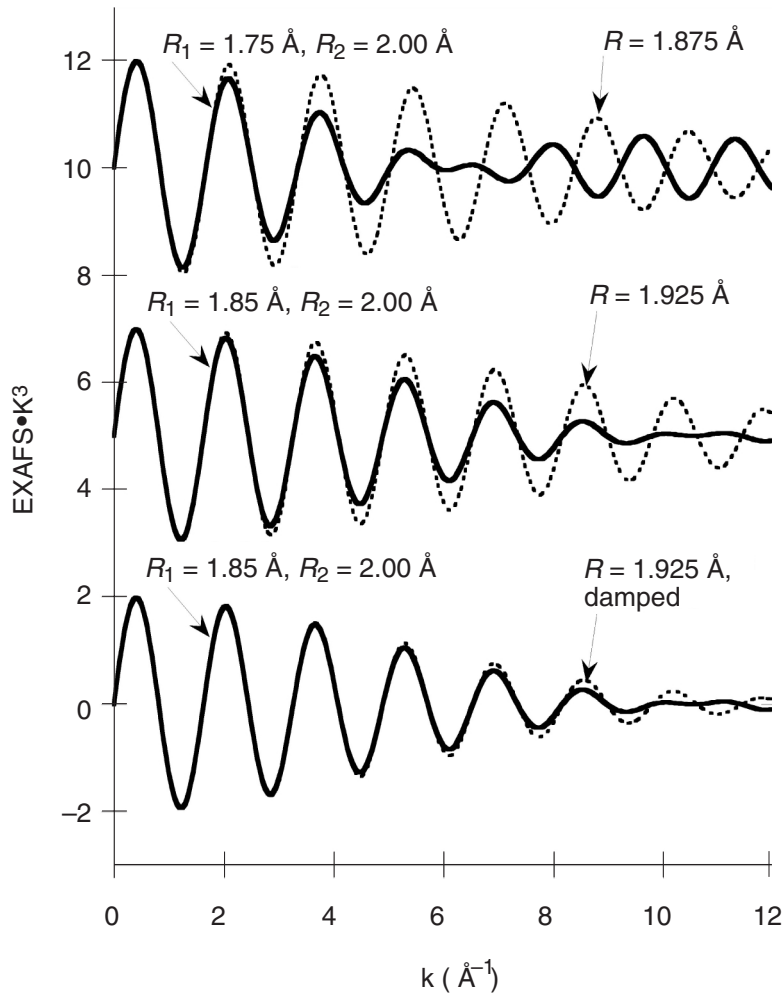

Figure 11 Simulated EXAFS data for one-shell (dashed line) and two-shell (solid line) models. In each case, the one-shell simulation has a distance equal to the average of the two-shell simulation. For the top and middle simulations, both one-shell and two-shell data use the same Debye–Waller factor. For the bottom simulation, the one-shell Debye–Waller factor has been increased to give the best agreement with the two-shell data. Two shells with a small Debye–Waller factor are, for any realistic noise level, indistinguishable from a single shell with a large Debye–Waller factor.

real (i.e., noisy) data, even though $\Delta R > \pi/2\Delta k$. This is because the Debye–Waller factor (σ^2 in Equation (3)) can mimic the damping that is caused by the presence of two shells of scatterers. This illustrates the fact that although the resolution limit of EXAFS is much better than those of most crystallography, it is nevertheless sufficiently poor that it is often not possible to resolve the contributions from different nearest neighbors, even when they are known chemically to be present at different distances.

CCC01063.0170 The definition of resolution is more complicated if there is more than one type of scattering atom. The presence of two different kinds of scattering atoms may increase the effective resolution. For example, the EXAFS signals for F and Cl have quite different $A_s(k)$ and $\phi_{as}(k)$. This means that F and Cl EXAFS signals *can* be resolved even if the distances are identical, although this can be complicated by destructive interference between the O and Cl signals.[65] Conversely, the presence of several different scatterers at about the same distance can change the apparent amplitude of an EXAFS feature, thus leading to misassignment of the chemical identity of the scatterer. For example, a Cu–Cu shell in the CuA site of cytochrome oxidase[74] was initially assigned as a Cu–S interaction[75–77] due to interference and the limited k range of the data.

1.59.2.4 Applications of EXAFS to Coordination Chemistry

CCC01063.0175 There are over 15,000 papers dealing with the application of X-ray absorption spectroscopy. Since the development of intense, readily accessible synchrotron sources in about 1980, there has been a steady growth in the applications of EXAFS (see Figure 12). Although the applications cover all areas of science, a significant fraction of these address questions of interest to coordination chemistry. Given the size of this literature, it is not realistic to report on all of the applications of EXAFS. In selecting the examples below, no attempt has been made to provide a comprehensive survey of the literature; a number of excellent reviews exist that survey different field-specific applications of EXAFS[27,78–91] together with several monographs on the subject.[86,92–94] Rather, the examples below have been selected to illustrate important types of applications.

1.59.2.4.1 De novo structure determination

CCC01063.0180 For de novo structure determination, one measures the EXAFS spectra for one or more of the atoms in a sample and uses this information to determine the structure around the absorbing atom. In principle this is straightforward, although in practice the analysis is often complicated by the limitations discussed above. It is seldom the case that EXAFS can provide reliable information for scatterers that are more than 5 Å from the absorbing atom and in most cases EXAFS provides little or no angular information. Despite these limitations, de novo structure determination remains one of the most important applications for EXAFS. The areas in which de novo structure determination are most important are those in which crystallography cannot be used. One key area is bioinorganic chemistry. It has been estimated that one-third of all proteins bind

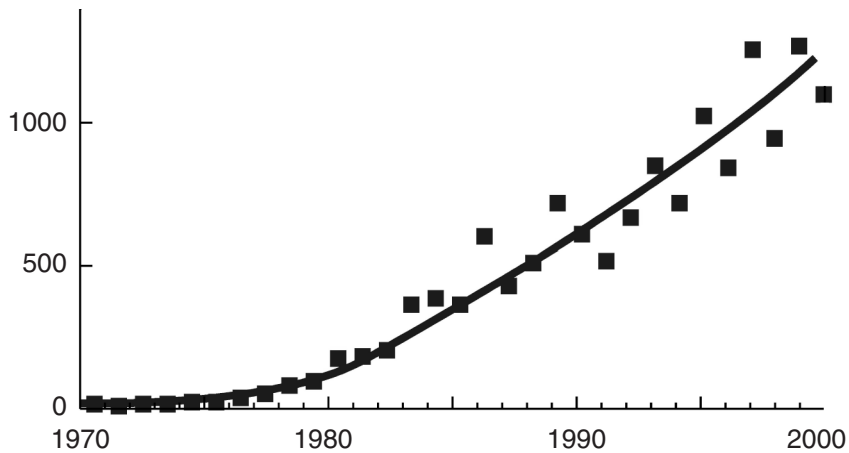

Figure 12 Number of XAS papers published per year. Solid line is a polynomial fit to the data.

metals. In many cases, the metal is at the active site, and thus structural characterization of the metal site is critical to a detailed understanding of the protein. Unfortunately, many proteins are difficult to crystallize, particularly when the form of interest is an unstable intermediate. Even when a protein *can* be crystallized, many protein crystal structures lack sufficient resolution to define the metal site accurately, and in some cases the metal site may be completely disordered. In these cases, EXAFS is the only technique that can provide direct structural information for the active site metal, and there are hundreds of examples of EXAFS being used to provide structural insight.[83,84,91,95]

CCC01063.0185 Exactly the same arguments make EXAFS a useful tool for materials chemistry, where many of the samples of interest are amorphous. Examples include studies of glasses,[96,97] of catalysts,[80,98–100] of liquids,[82,101–103] and of surfaces.[27,104–109] The limitations for amorphous samples are similar to those for biological samples, with the important additional complication that the metal of interest is typically not present in a single site but rather in an ensemble of sites. The EXAFS thus represents only the average structure and need not reflect the structure of any one of the individual absorbing sites.

1.59.2.4.2 Solution structure determination

CCC01063.0190 Although X-ray crystallography is extremely powerful as a structural probe, it only provides a description of the structure in the solid state. Since most chemical reactions take place in solution, determination of the solution structure is important for understanding reactivity. In some cases, for example in studies of transition metal cations dissolved in aqueous solution,[110–112] or for organometallics dissolved in solution,[68,113] EXAFS offers the only direct route for structure determination. In other cases, it is possible to crystallize the solute, but solution EXAFS is still important to determine if the crystallographic structure accurately represents the molecule of interest when it is dissolved in solution. The latter is particularly important for multinuclear aggregates, which might be expected to dissociate into smaller units when dissolved.[114] There have, to date, been relative few examples of EXAFS being used to determine solute structure, or to compare solute and crystalline structure. However, with the increased availability of synchrotron radiation, this is an area that is likely to grow in importance.

1.59.2.4.3 Resolution of crystallographic disorder

CCC01063.0195 Although most applications are to non-crystalline materials, EXAFS is also useful for characterizing the structure of metal ions in crystals. This is because crystallographic structure determination can suffer from resolution limitations analogous to those in EXAFS. In particular, the crystallographically determined structure for a metal ion that occupies a high symmetry site in a crystalline lattice is necessarily high symmetry, even though individual ions may have much lower symmetry. In such cases both X-ray diffraction, which gives the structure averaged over all unit cells, and XAS, which gives the structure averaged over all metal sites, may be necessary for a complete description of the structure. For example, the Jahn–Teller active Cu^{2+} may crystallize in a high symmetry site with six crystallographically identical bond lengths, in apparent violation of the Jahn–Teller theorem. EXAFS has been used to show[115] that the Cu site in bis[tris (2-pyridyl)methane]Cu^{2+} nitrate has the expected tetragonal distortion, with four short (2.04 Å) and two long (2.25 Å) Cu–N distances, despite the $\bar{3}$ symmetry of the crystallographic site, and to show[116] that $CuCl_6^{4-}$ ion in (3-chloroanilinium)$_8(CuCl_6)Cl_4$ has a conventional tetragonally elongated structure rather than the tetragonally compressed structure that had been suggested from the crystallography.[117]

CCC01063.0200 Similar concerns apply in studies of variable-composition crystals such as doped samples (e.g., high-T_c superconductors)[118–121] and ceramics.[122–126] Often, these samples are crystalline and have well-defined three-dimensional structures. However, the crystallographic structure gives only the average location of the major components of the crystal, and is insensitive to the location of the dopant ions. Moreover, crystallography, which reflects the structure averaged over all unit cells, may not give an accurate description of the local structure of the individual ions. For example, Vegard's law predicts a linear variation in lattice constant on going between composition extremes in a solid solution. EXAFS can be used to determine whether this variation is reproduced in the bond lengths around the individual components of the solid solution.[127,128] The combination of

EXAFS with crystallography thus provides a more detailed structural characterization than would be possible from either measurement alone.

1.59.2.4.4 Time-dependent structural evolution

CCC01063.0205 An exciting new development in XAS is the ability to measure time-resolved spectra. This provides a powerful tool for investigating the reactivity of solids in catalysis and solid-state chemistry.[129,130] To date, most studies have been limited to a time resolution of seconds although this can, in principle, extend into the femtosecond regime.[130,131] The latter offers the possibility of probing directly the structure of photoexcited states, thus following directly the structural changes that accompany a chemical.[132,133] Before this can be widely applied, more intense femtosecond X-ray sources are needed.[134] At present, time-resolved studies in the second to millisecond times are becoming relatively straightforward, and are providing important new chemical information.

CCC01063.0210 Although other probes may be substantially easier to use, XAS is sometimes the only method that is sensitive to the structures of interest, particularly for solid-state samples and *in situ* studies of catalysts.[135–138] For example, in a study of the reduction of NiO, time-resolved X-ray diffraction had shown that the catalyst went directly from $NiO \rightarrow Ni$ without a well-ordered intermediate phase,[137] but could not rule out the existence of an amorphous NiO_xphase, since the diffraction was not sensitive to disordered phases. However, the formation of an intermediate phase could be ruled out by time-resolved EXAFS. A similar situation exists for spectroscopically "silent" metals (d^{10} systems), which are difficult to probe with methods other than XAS. Examples that are important in bioinorganic chemistry include Cu^{+1} and Zn^{2+}. For carboxypeptidase, time-resolved XAS could be used to determine the rate of change of the native Zn^{2+} site, while conventional UV-visible methods could only be used on the Co^{2+} substituted enzyme.[139] The importance of XAS in both of these examples is as a tool for measuring rate constants.

CCC01063.0215 A second area where time-resolved EXAFS is important is for structural characterization of reactive intermediates. Reactive intermediates are difficult or impossible to crystallize. They may, however, be accessible to structural characterization by EXAFS. The difficulty is that a bulk technique such as EXAFS cannot easily be used to measure structure for minor components in a complex mixture. However, mathematical approaches such as principal component analysis[140–142] can be used to extract information about relatively minor components if a large enough number of individual spectra are measured. For example, in a study of the oxidation of *n*-butane over a V_2O_5 catalyst, hundreds of XAS spectra were measured with 1 second time resolution.[143] No single spectrum gave sufficient information that could be used to distinguish the different species that were present. However, by using principal component analysis, it was possible to identify contributions from three different species (one present at only ca. 20 mol.%) that contributed to the overall data variation. From comparison with standards, these components could be assigned to V^{5+}, V^{4+}, and V^{3+}.

CCC01063.0220 Time-resolved studies frequently make use of a dispersive geometry in which the synchrotron beam is focused onto the sample using a curved crystal,[144] as shown in Figure 13. In this geometry, the sample is illuminated with all X-ray energies simultaneously. The transmitted X rays are dispersed onto a position-sensitive detector, allowing much more rapid measurement of the spectrum. However, because this is a transmission geometry, dispersive measurements are limited to relatively concentrated samples; dilute samples require the fluorescence geometry shown in Figure 4. For fluorescence, the time resolution is limited to the speed with which the monochromator can be scanned. This is typically several seconds per scan, although there are recent advances in rapid-scanning monochromators that can extend this to the millisecond regime.[145,146] Extremely fast time resolution (nanosecond to femtosecond) requires a pump-probe experiment with a pulsed X-ray source.[130,131,133]

1.59.3 X-RAY ABSORPTION NEAR EDGE STRUCTURE

CCC01063.0225 A typical XANES spectrum is shown in Figure 14 (this is an expansion of the edge shown in Figure 2). It is clear that the XANES region is more complex than simply an abrupt increase in absorption cross-section. There are several weak transitions below the edge (pre-edge transitions) together with structured absorption on the high energy side of the edge. Some XANES spectra show intense narrow transitions on the rising edge (these can be much more intense than the transition at the edge in Figure 14). These are often referred to as "white lines" in reference to the fact that when film was used to record X-ray absorption spectra, an intense transition would

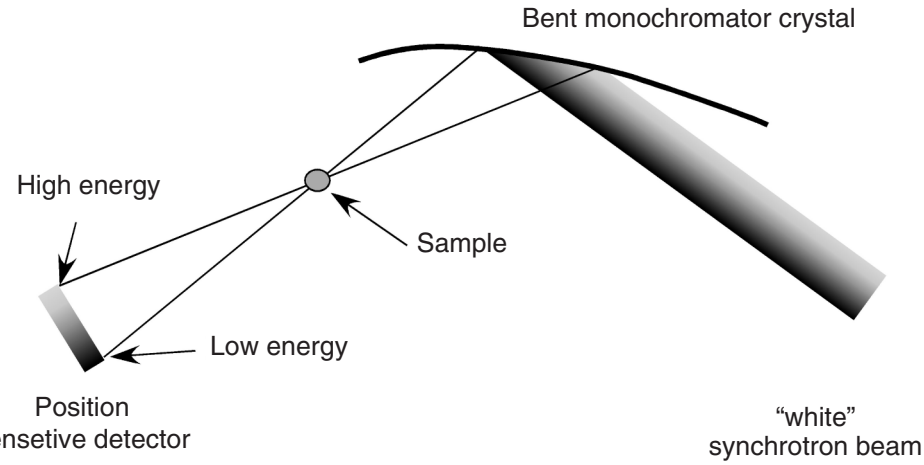

Figure 13 Dispersive XAS geometry. A broad band of X-ray energies is focused onto the sample using a curved crystal and detected using a position-sensitive detector. Time resolution is limited only by the readout time of the detector (microseconds in principle) but samples are limited to those accessible by transmission.

absorb all of the incident X rays, thus preventing the film from being exposed and leaving a white line on the film. Above the edge, there are a variety of structures that show generally oscillatory behavior, ultimately becoming the EXAFS oscillations.

CCC01063.0230 The same physical principles govern both the EXAFS region and the XANES region. However, in the near edge region the photoelectron has low kinetic energy, giving it a long mean-free path. In addition, the $\exp(-k^2)$ dependence of the Debye–Waller factor means that this damping factor is negligible in the XANES region. These effects combine to make the XANES region sensitive to longer distance absorber–scatterer interactions than are typically sampled by EXAFS. This greatly complicates simulation of XANES structure, since many interactions and a large number of multiple scattering pathways need to be included.[147–149] However, the sensitivity to multiple scattering is, at least in principle, an advantage since it provides the possibility of extracting information about the three-dimensional structure from XANES spectra. Although much progress has been made recently in the theoretical modeling of XANES,[111,112,147–150] most simulations of XANES structure remain qualitative. Nevertheless, the ability to make even qualitative fingerprint-like comparisons of XANES spectra can be important. If a representative library of reference spectra is available, spectral matching can be used to identify an unknown. Beyond this qualitative application, there are three main ways in which XANES spectra are used: to determine oxidation state, to deduce three-dimensional structure, and as a probe of electronic structure.

1.59.3.1 Sensitivity of XANES to Oxidation State

CCC01063.0235 The energy of an absorption edge is not well-defined. It can be taken as the energy at half-height or, more commonly, as the maximum in the first derivative with respect to energy. However, as

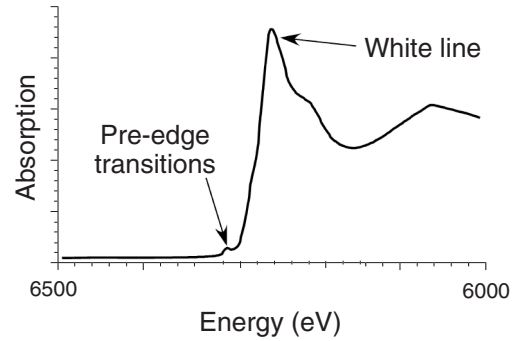

Figure 14 Expansion of the XANES region for the data shown in Figure 2, showing different features within the XANES region.

shown by Figure 14, edge spectra frequently have unresolved transitions superimposed on the rising edge. These will affect any attempt to define a unique "edge energy." Despite this ambiguity, edge energies have proven extremely useful in determining the oxidation state of the absorber. It has been known for many years that the energy of an edge increases as the oxidation state of the absorber increases.[151] This can be explained using an electrostatic model, since atoms with a higher oxidation state should have a higher charge, thus requiring more energetic X-ray to eject a core electron. An alternative interpretation of edge energies treats the edge features as "continuum resonances."[152] A continuum resonance involves excitation of a core electron into a high-energy state (above the continuum) that has a finite lifetime. An example is the potential well created by the absorbing and scattering (nearest neighbor) atoms. As the absorber–scatterer distance gets shorter, the energy of the continuum state increases as $1/R^2$. Since higher-oxidation-state metals have shorter bond lengths, both models predict an increase in edge energetic with increasing oxidation state. Regardless of which explanation is most appropriate, the phenomenological correlation between edge energy and oxidation state is well established, and is widely used in coordination chemistry.

1.59.3.2 Multiple Scattering and XANES

CCC01063.0240 As noted above, multiple scattering is particularly important in the XANES region. In principle, this means that it should be possible to determine the three-dimensional structure of the absorbing atom from analysis of the XANES features. Empirically, this is certainly the case; the XANES region is quite sensitive to small variations in structure, to the extent that two sites having identical EXAFS spectra can nevertheless have distinct XANES spectra.[65] This sensitivity is, at least in part, due to the fact that geometrical differences between sites alter the multiple scattering pathways, and thus the detailed structure in the immediate vicinity of the absorption edge. Although there has been progress in the interpretation of XANES spectra,[111,149] the agreement between calculated and observed spectra remains relatively poor in most cases. The development of theoretical and computational methods that will permit detailed interpretation of XANES spectra is one of the outstanding problems in the field.[153]

1.59.3.3 Bound State Transitions in XANES

CCC01063.0245 The weak pre-edge transitions (Figure 14) arise from bound state transitions. For the K edge of a first row transition metal, these arise from $1s \rightarrow 3d$ transitions, and are observed for every metal that has an open $3d$ shell.[154] Although the $1s \rightarrow 3d$ transition is forbidden by dipole selection rules, it is nevertheless observed due both to $3d + 4p$ mixing and to direct quadrupolar coupling.[155] The sensitivity to $3d + 4p$ mixing means that the intensity of the $1s \rightarrow 3d$ transition can be used as a probe of geometry, with the intensity increasing as the site is progressively distorted from a centrosymmetric environment (i.e., octahedral < square–pyramidal < tetrahedral)[156] or to distinguish between square–planar (i.e., centrosymmetric) and tetrahedral sites.[157] With careful analysis, the details of the $1s \rightarrow 3d$ transitions can be used to explore the electronic structure of the absorbing atom.[158]

CCC01063.0250 The analogous $1s \rightarrow 4d$ transition for second transition series metals is generally not observed. These edges occur at higher energy, where monochromator resolution is worse and core-hole lifetimes, which determine the intrinsic line width of a transition, are much shorter.[11] This results in broad edges for which the weak $1s \rightarrow 4d$ transitions are undetectable. However, for second row transition metals, it is still possible to obtain information about the empty bound states by measuring data at the L_3 and L_2 edges, which have $2p \rightarrow 4d$ transitions.[159] The low energy of these edges makes the transitions relatively sharp, and the $2p \rightarrow 4d$ transition is allowed, thus making these transitions intense. Similar spectroscopic advantages (narrow lines, allowed transitions) are found for L edge studies of the first transition series metals.[160,161] However, in this case the very low edge energy is experimentally challenging, requiring the use of ultra-high vacuum for the sample.

CCC01063.0255 In addition to excitations into the $3d$ (or $4d$) shells, XANES can also be used to probe higher-lying excited states. For atomic spectra, a complete series of "Rydberg" transitions can be seen.[162,163] For first transition series metals, the allowed $1s \rightarrow 4p$ transition is sometimes observed. This is the assignment given to the intense transition observed on the rising edge for Cu^{I} and for some square–planar Cu^{II} and Ni^{II} complexes. From studies of model compounds, it is found that the "$1s \rightarrow 4p$" transition is intense for square–planar complexes but weak for tetrahedral

complexes, as shown in Figure 15.[164,165] and thus can be used to deduce geometry. The greater intensity for square–planar complexes may be due to decreased mixing between the empty $4p$ orbital ($4p_z$) and the ligand orbitals. This intensity of the $1s \rightarrow 4p$ transition is even more dramatic for 2-coordinate Cu^{I}.[166]

CCC01063.0260 An alternative, complementary, approach to electronic structure information is to use ligand XANES rather than metal XANES. This is particularly promising as a tool for investigating sulfur or chlorine ligands[167–169] and has been used to quantitate the amount of metal–ligand orbital mixing (i.e., the covalency) of different complexes.[170] For example, excitation at the Cl K edge gives rise to an allowed $1s \rightarrow 3p$ transition. Since the Cl $3p$ orbitals are bonding orbitals in metal chlorides, the lowest energy transition at the Cl edge is actually a $1s$(Cl) $\rightarrow$ HOMO transition, where the HOMO has both metal $3d$ and Cl $3p$ character. The intensity of this transition is a direct measure of the percent $3p$ character of this orbital (i.e., the covalency of the complex). Ligand XANES can be more useful than metal XANES due to the fact that the transitions of interest from a bonding perspective are $1s \rightarrow 3p$ for S or Cl ligands and $1s \rightarrow 3d$ for a metal from the first transition series. The former is an allowed transition while the latter is forbidden by dipole selection rules, and consequently much weaker and harder to detect.

1.59.3.4 Multi-electron Transitions in XANES

CCC01063.0265 The single-electron bound-state transitions described above can be written as $\underline{1s}\,(V^*)^1$, where the underline in $\underline{1s}$ refers to a hole in the $1s$ orbital, and V* is a valence orbital. At higher photon energies, the X-ray has sufficient energy to excite an extra electron into the valence band (e.g., $V \rightarrow V^*$) resulting in double excitations such as $\underline{1s}\ \underline{V}\ V^{*2}$. In this notation, excitation of the core electron to the continuum is described as $\underline{1s}\ \varepsilon_p$, where ε_p indicates a p-symmetry photoelectron, with variable energy ε. The continuum states also have the possibility of multi-electron excitations, giving final states such as $\underline{1s}\ \underline{V}\ V^{*1}\ \varepsilon_p$. This class of multi-electron transition is sometimes referred to as shake-up transitions, to reflect the description of the excess energy as "shaking" a second electron into a higher-lying state.[171,172]

CCC01063.0270 In addition to shake-up transition, a second class of multi-electron transition is possible, as illustrated in Figure 16. Excitation of a core electron has the effect of converting an atom with atomic number Z into an atom with an apparent atomic number of $Z+1$. This means that, for example, in the $\underline{1s}4p^1$ state of Cu^{II}, the valence electrons experience the effective nuclear charge of Zn^{II}. The increased nuclear charge lowers the energy of the Cu^{II} $3d$ orbitals so that they are now lower than the ligand orbitals (B and C in Figure 16). Two transitions are now possible: the direct $\underline{1s}3d^9 4p^1$ transition (Figure 16B) and the multielectron transition to $\underline{1s}3d^{10}4p^1\underline{L}$, in which a ligand electron has been transferred to the lower-energy Cu $3d$ orbital. The latter gives a lower-energy excited state, and is often referred to as a shake-down transition. Shake-down transitions are seen frequently in photoelectron spectroscopy but have not been invoked often in XANES. One prominent exception is Cu^{II}, where polarized XANES spectra and theoretical calculations provide good evidence for shake-down transitions.[157,173–175] The large covalency of many Cu^{II} complexes

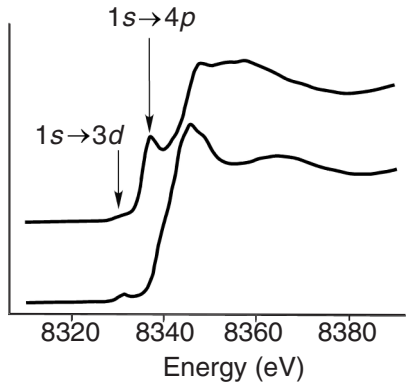

Figure 15 XANES spectra for 4-coordinate Ni^{II}, redrawn from data in Ref. 164. (top) Ni(cyclam) $(ClO_4)_2$ (square–planar) ; (bottom) $(Me_4N)_2NiCl_4$ (tetrahedral). Note the weaker $1s \rightarrow 3d$ transition and stronger $1s \rightarrow 4p$ transition for the square–planar site.

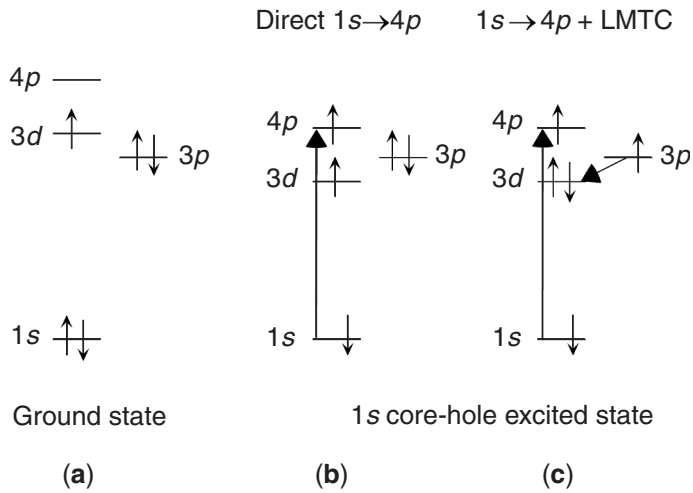

Figure 16 Schematic illustration of the energy levels involved in bound-state XANES features for 3*d* transition metals. For each diagram, metal orbitals (1*s*, 3*d*, 4*p*) are on the left and ligand orbitals (3*p*) are on the right. (a) Ground state; (b) 1*s* core-hole excited state showing direct $1s \rightarrow 4p$ transition; (c) 1*s* core-hole excited state showing multielectron $1s \rightarrow 4p$ plus ligand-to-metal charge transfer shake-down transition. Due to the higher effective charge of the core-hole excited state, the multielectron transition is at lower energy than the direct transition. The intensity of the shake-down transition is a measure of the covalency of the site (i.e., the metal $3d+$ ligand $3p$ mixing).

makes shake-down transitions more important here, but it seems likely that shake-down and other multielectron transtions[176] contribute to many XANES spectra.

1.59.3.5 Applications of XANES to Coordination Chemistry

CCC01063.0275 XANES spectra are much easier to measure than EXAFS spectra since even weak transitions are considerably more intense than EXAFS oscillations at high k. A second advantage of XANES spectra is that they can often be treated spectroscopically—that is, that individual spectral features can be attributed to specific features in the electronic structure. In contrast, EXAFS spectra are spectroscopically detected scattering patterns; it is not possible to attribute a specific EXAFS oscillation to a specific structural feature. Despite these advantages, and the fact that the XANES region is inevitably scanned during the process of measuring EXAFS spectra, relatively little use has been made of XANES beyond qualitative comparisons of an unknown spectrum to reference spectra. The most common qualitative use is for oxidation state assignment, although near-edge features have also been used to distinguish metal-site geometry (e.g., Figure 15).

CCC01063.0280 The complexity of XANES spectra, and in particular their sensitivity to multiple scattering from distant atoms, is largely responsible for the relatively limited attention that XANES spectra have received for quantitative analyses. With the development of new theoretical and computational approaches to XANES,[148,149,158,169,177] the utility of XANES for investigating coordination complexes is likely to increase.

1.59.4 HIGHER RESOLUTION XAS

CCC01063.0285 Despite the numerous applications of XAS, XAS spectra have, in general, quite limited resolution. For XANES, resolution limits are the consequence of relatively broad spectral lines and severe spectral overlap. Resolution can be improved, in some cases quite dramatically, by using polarization-dependent measurements to reduce spectral overlap (Section 1.59.4.1) or by using inelastic scattering (high-resolution fluorescence) to reduce line widths (Section 1.59.4.2). For EXAFS, one of the most serious resolution limitations results from the fact that EXAFS is sensitive to all of the absorber in a sample; if two different metal sites are present, EXAFS will give only the average structure. This can be addressed, in some cases, by using high-resolution fluorescence to

measure site-specific EXAFS spectra (Section 1.59.4.2), and in other cases by using spatially resolved EXAFS to resolve the EXAFS spectra from different absorbers (Section 1.59.4.3).

1.59.4.1 Polarization-dependent Measurements

CCC01063.0290 Synchrotron radiation is naturally polarized in the plane of the electron orbit. This can be used with oriented (typically single crystal) samples to make polarization-dependent measurements. In addition, it is possible to prepare circularly polarized X-ray beams, either by manipulating the properties of the electron orbit in the synchrotron[178,179] or by using the X-ray analog of a quarter-wave plate.[180,181]

1.59.4.1.1 Linearly polarized measurements

CCC01063.0295 Linear dichroism can be used to extract additional information from both EXAFS and XANES spectra.[182,183] For EXAFS, polarization-dependent measurements can add angular resolution to the normal EXAFS structural information,[184] allowing, for example, distinction between in-plane and axial bond lengths.[185,186] or detection of weak signals in the presence of strong signals by orienting the sample to minimize contributions from the strong signals.[187] Although often used with single crystals, polarized EXAFS can be used to determine the orientation dependence of the structure for any oriented sample. Examples of non-crystalline orientation include studies probing the structure of substrates adsorbed on surfaces, [188] the orientation of dye molecules in Langmuir–Blodgett films,[189] and the orientation of metal active sites in protein multilayers[190,191] and monolayers.[192]

CCC01063.0300 Polarized XANES measurements have similar advantages to polarized EXAFS, and have been widely used to determine the orientation of the absorber. A second use of polarized XANES is to determine the symmetry properties of particular edge features, and thus to limit the possible interpretation of particular transitions.[165,175,193,194] For example, the observation of fourfold periodicity was used to prove that the $1s \rightarrow 3d$ transitions in first row transition metals arise from direct quadrupolar coupling.[155,195]

1.59.4.1.2 X-ray MCD

CCC01063.0305 If a circularly polarized X-ray beam is used, it is possible to measure the circular dichroism (CD) of a sample. By far the most important use is to study the circular dichroism that is induced by application of a magnetic field, i.e., magnetic circular dichroism (MCD). Just as in the UV-visible region, X-ray MCD makes use of the fact that the energy of an orbital will vary depending on relative orientation of the local and the applied magnetic field. This allows one to measure element-selective magnetic properties of a sample, since each element can be probed independently. X-ray MCD spectra can be used to deduce the local spin and orbital moments of an atom.[196–198]

CCC01063.0310 Although most widely used for studies of magnetic materials, it is also possible to use X-ray MCD to study metal sites in proteins.[199] Although X-ray MCD is most often used to study XANES features, it can also be used to probe EXAFS. In this case, the dichroic signal is limited to scattering atoms that are affected by the magnetic field. This can be used to enhance the detectability of the EXAFS signal from a small number of magnetic neighbors in the presence of a large EXAFS signal from non-magnetic scatterers.[200–202]

1.59.4.1.3 Natural circular dichroism

CCC01063.0315 Very recently, it has been shown that it is also possible to measure natural (i.e., non-magnetic) circular dichroism for X-ray absorption.[203] For crystals of $Na_3Nd(digly)_3{\cdot}2NaBF_4{\cdot}6H_2O$, the dissymmetry, $(A_L - A_R)/(A_L + A_R)$, is approximately 10^{-3}, comparable to dissymmetries seen in UV-visbile CD spectra. However, for crystals of $2[Co(en)_3Cl_3]{\cdot}NaCl{\cdot}6H_2O$ there is an amazing dissymmetry of 12.5% in the vicinity of the $1s \rightarrow 3d$ pre-edge transition.[204] This can be understood by considering the origin of circular dichroism. Differential absorption of left and right circularly polarized light is due to odd-parity interference between different photon–molecule interaction

operators. In the UV-visible region, CD is dominated by the interference between the electric and magnetic dipole transition moments. However, CD can also arise from interference between electric dipole and electric quadrupole terms, and this is the dominant source of CD in the X-ray region. For transitions such as $1s \rightarrow 3d$, which are quadrupole allowed and dipole forbidden, the X-ray CD is extremely large. X-ray CD thus provides a unique tool for investigating the origin of specific edge features. In addition, X-ray CD can significantly enhance the resolution of edge features. For example, the dipole-forbidden $2p \rightarrow 4f$ transition at the Nd L_3 edge of $Na_3Nd(digly)_3$ appears only as an extremely weak shoulder on the low-energy side of the allowed white-line transitions ($2p \rightarrow nd$). However, in the CD spectrum of $Na_3Nd(digly)_3$, only the $2p \rightarrow 4f$ transition is seen, allowing this feature to be readily distinguished from the white line.

CCC01063.0320 In addition to core $\rightarrow$ valence transitions, it is also possible to observe X-ray CD at higher energy, in the XANES and EXAFS regions. Single-scattering terms, which dominate the X-ray photoabsorption cross-section, cannot give rise to circular dichroism. Consequently, X-ray CD spectra are sensitive only to multiple scattering and not to single scattering.[205,206] This dramatically simplifies interpretation of the spectra and has the added benefit that simulations of X-ray CD are often better than the corresponding simulations of X-ray absorption, since the inelastic effects that complicate interpretation of the absorption do not survive in the CD.[203,207] Since multiple-scattering terms are sensitive to geometry, X-ray CD is a very sensitive probe of three-dimensional structure. In addition, from the sign of the CD, it is possible to distinguish between enantiomers.

1.59.4.2 High-resolution X-ray Fluorescence

CCC01063.0325 As discussed above, XAS is frequently measured as fluorescence excitation spectra. Typically, this involves collecting all of the X-ray fluorescence, with little or no energy discrimination, and the discussion thus far has ignored the structure that is observed in emission spectra. However, it is possible to use a high-resolution fluorescence monochromator to give energy resolution <1 eV. Such measurements, which can be described as X-ray inelastic scattering, reveal a wealth of structural detail in the emission spectra. Detailed discussion of emission spectra is beyond the scope of this review, but has been treated elsewhere.[208] For the present discussion, there are two important consequences of high-resolution measurements; these can be used to enhance the resolution of absorption edges and to give site-selective XAS data.

1.59.4.2.1 Elimination of lifetime broadening in XANES

CCC01063.0330 XANES spectra frequently have very broad features due to the intrinsic broadening from the core-hole lifetime, which may be as much as 5–10 eV for L edges. By monitoring emission with high resolution, one samples only a small subset of the excited states and thus effectively eliminates broadening from the core-hole. For $Dy(NO_3)_3$, the L_3 lifetime broadening is ca. 5 eV and the $L_{\alpha 1}$ (L_3M_5) emission line has a width of nearly 10 eV. By monitoring a narrow band (ca. 0.3 eV) from within $L_{\alpha 1}$ emission band, the resolution of the excitation spectrum was dramatically enhanced.[209] In the sharpened spectrum, the resolution is effectively governed by the lifetime of the M_5 state that gives rise to the emission rather than by the much shorter lifetime of the excited L_3 state.[208] Measurements using high-resolution emission are much more challenging than conventional X-ray absorption, since the high-resolution of the fluorescence monochromator results in a much weaker signal. This requires an extremely intense X-ray beam and consequently high-resolution measurements are more sensitive to radiation damage. Nevertheless, for certain samples, the experimental difficulties are more than compensated for by the ability to resolve transitions that would be otherwise unresolvable.

1.59.4.2.2 Site-selective XAS

CCC01063.0335 If emission spectra are measured with sufficiently high resolution, it is found that emission energies correlate both with oxidation state and with spin state.[208] Consequently, high-resolution emission offers the possibility of distinguishing the XAS spectra for different absorbing sites. For example, Fe^{2+} and Fe^{3+} have slightly different emission spectra. By tuning the fluorescence

analyzer to energies dominated by one or the other oxidation state, it was possible to measure valence-selective EXAFS spectra for Prussian Blue, $Fe^{3+}{}_4(Fe^{2+}(CN)_6)_3$.[210] This possibility of measuring site-selective EXAFS has the potential to significantly simplify the interpretation of EXAFS data for complex mixtures.[211] In a related experiment, it was possible to measure spin-selective XANES spectra for MnF_2 by monitoring a satellite on the low-energy side of the K_β emission line.[212] The satellite arises because of the fact that the K_β ($3p \rightarrow 1s$) energy varies depending on whether the spin of the $3p^5$ shell (created by the K_β emission) is parallel or anti-parallel to the spin of the $3d^5$ shell. This makes it possible to distinguish spin-up excitations (photoelectron has spin parallel to the $3d^5$ shell) from spin-down excitations and thus to obtain magnetic information similar to that obtained by X-ray MCD, but without the need for an applied magnetic field.

1.59.4.3 Spatially Resolved Measurements

CCC01063.0340 Another way to improve the resolution of XAS is to add spatial resolution.[213] With modern synchrotron facilities, it is relatively straightforward to record XAS spectra using a 1 μm × 1 μm beam.[214,215] These so-called X-ray microprobe beams can be used for all of the XANES and EXAFS experiments discussed above, but with the added benefit of permitting spatially resolved measurements. In addition, it is possible to construct a true soft X-ray microscope with spatial resolution (30–50 nm) close to the diffraction limit of light.[216] X-ray microscopy provides many of the benefits of electron microscopy, with the advantage of lower sample damage and greater tolerance of wet samples but does not usually involve spectroscopic measurements. The emphasis here is on X-ray spectroscopy using X-ray microprobe beams.

1.59.4.3.1 Methods for focusing X rays

CCC01063.0345 In the simplest X-ray microprobe implementation, slits or a pinhole can be used to limit the size of the beam. Although easy to implement and widely used, this approach greatly reduces the available photon flux and is thus limited to concentrated samples and relatively poor spatial resolution.[213] A variety of schemes can be used to focus the X-ray beam prior to (or in place of) beam-defining slits.[217]

CCC01063.0350 Conventional focusing optics require a material that is both transparent and significantly refractive. This is difficult to accomplish in the X-ray region since the refractive index of most materials is extremely close to 1 in the X-ray region. There has been recent progress in designing compound refractive X-ray lenses, in which multiple lenses are used to compensate for the small focusing power of each lens.[218] However, most X-ray microprobes rely on reflective or diffractive optics. Although X rays are not reflected at normal incidence, they do undergo total external reflection at a sufficiently grazing angle of incidence. The widely used Kirkpatrick–Baez geometry uses a pair of curved mirrors set perpendicular to one another in order to minimize the astigmatism of a single curved mirror. This can provide spot sizes of a few μm when used with modern synchrotron sources. Capillary optics rely on total external reflection of an X-ray beam propagating inside of a capillary. These can give spatial resolutions as small as 50 nm, but suffer from extremely high divergence, necessitating that the sample be placed very close (<100 μm) to the capillary. Bragg diffraction, which is used for X-ray monochromators, can also be used to focus an X-ray beam by using a curved crystal. Fresnel zone plates are a diffractive optical element, made up of alternating concentric circular zones. With modern microfabrication, the minimum attainable zone width (which determines the spatial resolution) is approximately 20 nm in the soft X-ray region and closer to 100 nm in the hard X-ray region (due to the need for thicker zones in order to have sufficient contrast in the hard X-ray regime). Unfortunately, zone plates are a chromatic optical element and must be refocused if the energy is changed, thus limiting their use for spectroscopic measurements.

1.59.4.3.2 Applications of X-ray microprobes

CCC01063.0355 X-ray microprobe studies to date have concentrated mostly on geological and environmental samples. If the sample of interest is very small, for example because it is contained in a diamond

anvil cell, the X-ray microprobe may be required to obtain high-quality data.[219] More frequently, the microprobe is required because the sample is heterogeneous. In these cases, the X-ray microprobe can be used to measure XAS spectra selectively for different parts of the sample. This was used, for example, to study the different types of Au present in arsenopyrite ore[220] and to define the U oxidation state associated with spatially resolved uranium precipitates in U-contaminated soils.[221] In these examples, the microprobe beam simplifies interpretation of the spectra by permitting measurements on a distance scale at which the sample is homogeneous. Alternatively, known spectral differences, for example between chromate and Cr^{3+},[222] or between Se^{6+} and elemental Se[215] can be used in conjunction with microprobe imaging to follow the evolution of a sample, for example during the course of a reaction.

1.59.5 REFERENCES

1. Bearden, J. A.; Burr, A. F. *Rev. Mod. Phys.* **1967**, *39*, 125–142.
2. James, R. W. *The Optical Principles of the Diffraction of X-ray*; Ox Bow Press, 1982.
3. X-ray optical constants, Center for X-ray Optics, Lawrence Berkeley Laboratory. http://www-cxro.lbl.gov/optical_constants/web.html.
4. NIST Physical Reference Data. http://physics.nist.gov/PhysRefData/XrayMassCoef/cover.html.
5. Moseley, H. G. J. *Phil. Mag.* **1914**, *27*, 703–714.
6. Moseley, H. G. J. *Phil. Mag.* **1913**, *26*, 1024–1034.
7. Markowicz, A. A. In *Handbook of X-ray Spectrometry*; 2nd ed.; Van Grieken, R. E., Markowicz, A. A., Eds.; Marcel Dekker: New York, 2002.
8. Compton, A. H.; Allison, S. K. *X rays in Theory and Experiment*; 2nd ed.; D. Van Nostrand Company: Princeton, 1935.
9. *X-ray Data Booklet*, 2nd ed.; Thompson, A. C.; Vaughan, D. Eds.; Lawrence Berkeley National Laboratory: Berkeley, 2001.
10. Bearden, J. A. *Rev. Mod. Phys.* **1967**, *39*, 78.
11. Krause, M. O.; Oliver, J. H. *J. Phys. Chem. Ref. Data* **1979**, *8*, 329.
12. Pettifer, R. F.; Borowski, M.; Loeffen, P. W. *J. Synchrot. Radiat.* **1999**, *6*, 217–219.
13. Jaklevic, J.; Kirby, J. A.; Klein, M. P.; Robertson, A. S.; Brown, G. S.; Eisenberger, P. *Solid State Commun.* **1977**, *23*, 679–682.
14. Goulon, J.; Goulonginet, C.; Cortes, R.; Dubois, J. M. *J. Physique* **1982**, *43*, 539–548.
15. Stern, E. A.; Elam, W. T.; Bunker, B. A.; Lu, K.; Heald, S. M. *Nucl. Instrum. Methods Phys. Res.* **1982**, *195*, 345–346.
16. Stern, E. A.; Heald, S. M. *Rev. Sci. Instrum.* **1979**, *50*, 1579–1582.
17. Cramer, S. P.; Tench, O.; Yocum, M.; George, G. N. *Nucl. Instrum. Methods Phys. Res. Sect. A-Accel. Spectrom. Dect. Assoc. Equip.* **1988**, *266*, 586–591.
18. Furenlid, L. R.; Kraner, H. W.; Rogers, L. C.; Cramer, S. P.; Stephani, D.; Beuttenmuller, R. H.; Beren, J. *Nucl. Instrum. Methods Phys. Res. Sect. A-Accel. Spectrom. Dect. Assoc. Equip.* **1992**, *319*, 408–413.
19. Ellis, A. T. In *Handbook of X-ray Spectrometry*; 2nd ed.; Van Grieken, R. E., Markowicz, A. A., Eds.; Marcel Dekker: New York, 2002.
20. Zhang, K.; Rosenbaum, G.; Bunker, G. *J. Synchrot. Radiat.* **1998**, *5*, 1227–1234.
21. Helsen, J. A.; Kuczumow, A. In *Handbook of X-ray Spectrometry*; 2nd ed.; Van Grieken, R. E., Markowicz, A. A., Eds.; Marcel Dekker: New York 2002.
22. Emura, S.; Moriga, T.; Takizawa, J.; Nomura, M.; Bauchspiess, K. R.; Murata, T.; Harada, K.; Maeda, H. *Phys. Rev. B* **1993**, *47*, 6918–6930.
23. Goulon, J.; Tola, P.; Brochon, J. C.; Lemonnier, M. *Acta Crystallogr. Sect. A* **1984**, *40*, C394–C394.
24. Tola, P.; Retournard, A.; Dexpertghys, J.; Lemonnier, M.; Pagel, M.; Goulon, J. *Chem. Phys.* **1983**, *78*, 339–345.
25. Stohr, J.; Jaeger, R.; Brennan, S. *Surf. Sci.* **1982**, *117*, 503–524.
26. Stohr, J. *Jpn J Appl Phys* **1978**, *17*, 217–220.
27. Haase, J. *J. Chem. Soc.-Faraday Trans.* **1996**, *92*, 1653–1667.
28. Schroeder, S. L. M.; Moggridge, G. D.; Ormerod, R. M.; Rayment, T.; Lambert, R. M. *Surf. Sci.* **1995**, *324*, L371–L377.
29. Röntgen, W. C. *Nature* **1896**, *53*, 274.
30. Storage Ring Synchrotron Radiation Sources. www-ssrl.slac.stanford.edu/sr-source.html.
31. Stern, E. A.; Sayers, D. E.; Lytle, F. W. *Phys. Rev. B* **1975**, *11*, 4836–4846.
32. Lee, P. A.; Pendry, J. B. *Phys. Rev. B* **1975**, *11*, 2795–2811.
33. Ashley, C. A.; Doniach, S. *Phys. Rev. B* **1975**, *11*, 1279–1288.
34. Teo, B. K.; Lee, P. A.; Simons, A. L.; Eisenberger, P.; Kincaid, B. M. *J. Am. Chem. Soc.* **1977**, *99*, 3854–3856.
35. Lee, P. A.; Teo, B. K.; Simons, A. L. *J. Am. Chem. Soc.* **1977**, *99*, 3856–3859.
36. Lee, P. A.; Teo, B. K.; Simons, A. L. *Bull. Am. Phys. Soc.* **1977**, *22*, 319–319.
37. Strange, R. W.; Blackburn, N. J.; Knowles, P. F.; Hasnain, S. S. *J. Am. Chem. Soc.* **1987**, *109*, 7157–7162.
38. Teo, B. K. *J. Am. Chem. Soc.* **1981**, *103*, 3990–4001.
39. Rehr, J. J.; Albers, R. C.; Zabinsky, S. I. *Phys. Rev. Lett.* **1992**, *69*, 3397–400.
40. Wang, S.; Lee, M. H.; Hausinger, R. P.; Clark, P. A.; Wilcox, D. E.; Scott, R. A. *Inorg. Chem.* **1994**, *33*, 1589–1593.
41. Binsted, N.; Strange, R. W.; Hasnain, S. S. *Biochemistry* **1992**, *31*, 12117–12125.
42. Boswell, J. S.; Reedy, B. J.; Kulathila, R.; Merkler, D.; Blackburn, N. J. *Biochemistry* **1996**, *35*, 12241–12250.
43. Chaboy, J.; Marcelli, A.; Tyson, T. A. *Phys. Rev. B* **1994**, *49*, 11652–11661.
44. Dangelo, P.; Nolting, H. F.; Pavel, N. V. *Phys. Rev. A* **1996**, *53*, 798–805.
45. Filipponi, A.; Dicicco, A. *Phys. Rev. A* **1995**, *52*, 1072–1078.

46. Dangelo, P.; Pavel, N. V.; Roccatano, D.; Nolting, H. F. *Phys. Rev. B* **1996**, *54*, 12129–12138.
47. D'Angelo, P.; Pavel, N. V.; Borowski, M. *J. Synchrot. Radiat.* **2001**, *8*, 666–668.
48. Dubiel, M.; Brunsch, S.; Arcon, I.; Frahm, R. *J. Physique* **1997**, *7*, 1169–1170.
49. Wende, H.; Baberschke, K. *J. Electron Spectrosc. Relat. Phenom.* **1999**, *103*, 821–826.
50. Wende, H.; Srivastava, P.; Chauvistre, R.; May, F.; Baberschke, K.; Arvanitis, D.; Rehr, J. J. *J. Phys.-Condes. Matter* **1997**, *9*, L427–L433.
51. Ankudinov, A. L.; Conradson, S. D.; de Leon, J. M.; Rehr, J. J. *Phys. Rev. B* **1998**, *57*, 7518–7525.
52. Ankudinov, A. L.; Rehr, J. J.; Low, J.; Bare, S. R. *Phys. Rev. Lett.* **2001**, *86*, 1642–1645.
53. Michalowicz, A.; Vlaic, G. *J. Synchrot. Radiat.* **1998**, *5*, 1317–1320.
54. Rehr, J. J.; Booth, C. H.; Bridges, F.; Zabinsky, S. I. *Phys. Rev. B.* **1996**, *53*, 9468–9470.
55. Filipponi, A.; DiCicco, A. *Phys. Rev. B* **1996**, *53*, 9466–9467.
56. Sanchez del Rio, M.; San Miguel, A. ESRF XAFS Software database. http://www.esrf.fr/computing/scientific/exafs/intro.html.
57. Rehr, J. J.; Mustre, d. L. J.; Zabinsky, S. I.; Albers, R. C. *J. Am. Chem. Soc.* **1991**, *113*, 5135–5140.
58. Rehr, J. J.; Albers, R. C. *Rev. Mod. Phys.* **2000**, *72*, 621–654.
59. Gurman, S. J.; Binsted, N.; Ross, I. *J. Phys. C.* **1986**, *19*, 1845–1861.
60. Filipponi, A.; DiCicco, A.; Natoli, C. R. *Phys. Rev. B* **1995**, *52*, 15122–15134.
61. Filipponi, A.; DiCicco, A. *Phys. Rev. B* **1995**, *52*, 15135–15149.
62. Dicicco, A. *Physica B* **1995**, *209*, 125–128.
63. Vaarkamp, M.; Dring, I.; Oldman, R. J.; Stern, E. A.; Koningsberger, D. C. *Phys. Rev. B.* **1994**, *50*, 7872–7883.
64. Bunker, G.; Hasnain, S.; Ayers, D. In *X-ray Absorption Fine Structure*; Hasnain, S. S., Ed., Ellis Horwood: New York, 1991.
65. Clark-Baldwin, K.; Tierney, D. L.; Govindaswamy, N.; Gruff, E. S.; Kim, C.; Berg, J.; Koch, S. A.; Penner-Hahn, J. E. *J. Am. Chem. Soc.* **1998**, *120*, 8401–8409.
66. Riggs-Gelasco, P. J.; Mei, R.; Yocum, C. F.; Penner-Hahn, J. E. *J. Am. Chem. Soc.* **1996**, *118*, 2387–2399.
67. Sayers, D. E.; Stern, E. A.; Lytle, F. W. *Phys. Rev. Lett.* **1971**, *27*, 1204.
68. Stemmler, T. L.; Barnhart, T.; Penner-Hahn, J. E.; Tucker, C. E.; Knochel, P.; Böhme, M.; Frenking, G. *J. Am. Chem. Soc.* **1995**, *117*, 12489–12497.
69. Riggs-Gelasco, P. J.; Stemmler, T. L.; Penner-Hahn, J. E. *Coord. Chem. Rev.* **1995**, *144*, 245–286.
70. Stern, E. A. *Phys. Rev. B.* **1993**, *48*, 9825–9827.
71. Michalowicz, A.; Provost, K.; Laruelle, S.; Mimouni, A.; Vlaic, G. *J. Synchrot. Radiat.* **1999**, *6*, 233–235.
72. Stern, E. A. *Jpn. J. Appl. Phys.* **1993**, *1*, 851–855.
73. Lee, P. A.; Citrin, P. H.; Eisenberger, P.; Kincaid, B. M. *Rev. Mod. Phys* **1981**, *53*, 769–806.
74. Blackburn, N. J.; Barr, M. E.; Woodruff, W. H.; van der Ooost, J.; de Vries, S. *Biochemistry* **1994**, *33*, 10401–10407.
75. Scott, R. A.; Zumft, W. G.; Coyle, C. L.; Dooley, D. M. *Proc. Natl. Acad. Sci. USA* **1989**, *86*, 4082–4086.
76. Dooley, D. M.; McGuirl, M. A.; Rosenzweig, A. C.; Landin, J. A.; Scott, R. A.; Zumft, W. G.; Devlin, F.; Stephens, P. J. *Inorg. Chem.* **1991**, *30*, 3006–3011.
77. George, G. N.; Cramer, S. P.; Frey, T. G.; Prince, R. C. *Biochim. Biophys. Acta* **1993**, *1142*, 240–252.
78. Penner-Hahn, J. E. *Coord. Chem. Rev.* **1999**, *192*, 1101–1123.
79. Bertagnolli, H.; Ertel, T. S. *Angew. Chem.-Int. Edit. Engl.* **1994**, *33*, 45–66.
80. Alexeev, O.; Gates, B. C. *Top. Catal.* **2000**, *10*, 273–293.
81. Bazin, D.; Guczi, L. *Appl. Catal. A-Gen.* **2001**, *213*, 147–162.
82. Filipponi, A. *J. Phys.-Condes. Matter* **2001**, *13*, R23–R60.
83. Garner, C. D. *Adv. Inorg. Chem.* **1991**, *36*, 303–339.
84. Scott, R. A. *Methods Enzymol.* **1985**, *117*, 414–459.
85. Sharpe, L. R.; Heineman, W. R.; Elder, R. C. *Chem. Rev.* **1990**, *90*, 705–722.
86. Teo, B. K. *EXAFS: Basic Principles and Data Analysis*; Springer-Verlag: New York, 1986.
87. Grady, B. P. *Microchem J.* **2002**, *71*, 267–279.
88. Johnston, P.; Wells, P. B. *Radiat. Phys. Chem.* **1995**, *45*, 393–412.
89. Linford, R. G. *Chem. Soc. Rev.* **1995**, *24*, 267.
90. Parsons, J. G.; Aldrich, M. V.; Gardea-Torresdey, J. L. *Appl. Spectrosc. Rev.* **2002**, *37*, 187–222.
91. Penner-Hahn, J. E. *ACS Symposium Series* 1988, *372*, 28–48.
92. Stöhr, J. *NEXAFS Spectroscopy*; Springer: Berlin, 1992.
93. Koningsberger, D. C.; Prins, R. Eds.; *X-ray Absorption: Principles, Applications, Techniques of EXAFS SEXAFS, and XANES*; John Wiley & Sons: New York, 1988; Vol. 91.
94. Teo, B. K.; Joy, D. C. Eds.; *EXAFS [Extended X-Ray Absorption Fine Structure] Spectroscopy: Techniques and Applications*; Plenum Press: New York, 1981.
95. Cramer, S. P. *Chem. Anal.* **1988**, *92*, 257–320.
96. Yamanaka, T.; Nagai, T.; Tsuchiya, T. *Z. Kristall.* **1997**, *212*, 401–410.
97. Gleiter, H. *Adv. Mater.* **1992**, *4*, 474–481.
98. Shido, T.; Prins, R. *Curr. Opin. Solid State Mat. Sci.* **1998**, *3*, 330–335.
99. Evans, J. *Chem. Soc. Rev.* **1997**, *26*, 11–19.
100. Thomas, J. M.; Sankar, G. *Acc. Chem. Res.* **2001**, *34*, 571–581.
101. Minicucci, M.; DiCicco, A. *J. Physique* **1997**, *7*, 1027–1028.
102. DiCicco, A.; Minicucci, M.; Filipponi, A. *Phys. Rev. Lett.* **1997**, *78*, 460–463.
103. DiCicco, A. *Phys. Rev. B* **1996**, *53*, 6174–6185.
104. Sinfelt, J. H. *Surf. Sci.* **2002**, *500*, 923–946.
105. Scheidegger, A. M.; Sparks, D. L. *Soil Sci.* **1996**, *161*, 813–831.
106. Randall, S. R.; Sherman, D. M.; Ragnarsdottir, K. V.; Collins, C. R. *Geochim. Cosmochim. Acta* **1999**, *63*, 2971–2987.
107. Ohta, T.; Yokoyama, T.; Terada, S.; Imanishi, A.; Kitajima, Y. *Res. Chem. Intermed.* **2000**, *26*, 29–43.
108. Stohr, J. *Bull. Am. Phys. Soc.* **1980**, *25*, 323–323.
109. Hubbard, A. T. *Heterogeneous Chem. Rev.* **1994**, *1*, 3–39.

110. D'Angelo, P.; Barone, V.; Chillemi, G.; Sanna, N.; Meyer-Klaucke, W.; Pavel, N. V. *J. Am. Chem. Soc.* **2002**, *124*, 1958–1967.
111. D'Angelo, P.; Benfatto, M.; Della Longa, S.; Pavel, N. V. *Phys. Rev. B* **2002**, *66*, art. no.-064209.
112. Benfatto, M.; D'Angelo, P.; Della Longa, S.; Pavel, N. V. *Phys. Rev. B* **2002**, *65*, art. no.-174205.
113. Barnhart, T. M.; Huang, H.; Penner-Hahn, J. E. *J. Org. Chem* **1995**, *60*, 4310–4311.
114. Lah, M. S.; Gibney, B. R.; Tierney, D. L.; Penner-Hahn, J. E.; Pecoraro, V. L. *J. Am. Chem. Soc.* **1993**, *115*, 5857–5858.
115. Astkey, T.; Ellis, P. J.; Freeman, H. C.; Hitchman, M. A.; Keene, F. R.; Tiekink, E. R. T. *J. Chem. Soc., Dalton Trans.* **1995**, 595–601.
116. Ellis, P. J.; Freeman, H. C.; Hitchman, M. A.; Reinen, D.; Wagner, B. *Inorg. Chem.* **1994**, *33*, 1249–1250.
117. Tucker, D.; White, P. S.; Trojan, K. L.; Kirk, M. L.; Hatfield, W. E. *Inorg. Chem.* **1991**, *30*, 823.
118. Wu, Z. Y.; Saini, N. L.; Bianconi, A. *Phys. Rev. B* **2001**, *6409*, art. no.-092507.
119. Oyanagi, H.; Saini, N. L.; Bianconi, A. *Int. J. Mod. Phys. B* **2000**, *14*, 3623–3631.
120. Dimitrov, D. A.; Ankudinov, A. L.; Bishop, A. R.; Conradson, S. D. *Phys. Rev. B* **1998**, *58*, 14227–14237.
121. Conradson, S. D. *Appl. Spectrosc.* **1998**, *52*, 252A–279A.
122. Mastelaro, V. R.; Briois, V.; de Souza, D. P. F.; Silva, C. L. *J. European Ceram. Soc.* **2003**, *23*, 273–282.
123. Winterer, M.; Delaplane, R.; McGreevy, R. *J. Appl. Crystallogr.* **2002**, *35*, 434–442.
124. Li, P.; Chen, I. W.; Pennerhahn, J. E. *Phys. Rev. B* **1993**, *48*, 10063–10073.
125. Li, P.; Chen, I. W.; Pennerhahn, J. E. *Phys. Rev. B* **1993**, *48*, 10074–10081.
126. Li, P.; Chen, I. W.; Pennerhahn, J. E. *Phys. Rev. B* **1993**, *48*, 10082–10089.
127. Scheinost, A. C.; Stanjek, H.; Schulze, D. G.; Gasser, U.; Sparks, D. L. *Am. Miner.* **2001**, *86*, 139–146.
128. Lebedev, A. I.; Sluchinskaya, I. A.; Demin, V. N.; Munro, I. *Phys. Solid State* **1999**, *41*, 1275–1282.
129. Ressler, T.; Wienold, J.; Jentoft, R. E.; Neisius, T.; Gunter, M. M. *Top. Catal.* **2002**, *18*, 45–52.
130. Coppens, P.; Novozhilova, I. V. *Faraday Discuss.* **2003**, *122*, 1–11.
131. Bressler, C.; Saes, M.; Chergui, M.; Grolimund, D.; Abela, R.; Pattison, P. *J. Chem. Phys.* **2002**, *116*, 2955–2966.
132. Chen, L. X. *J. Electron Spectrosc. Relat. Phenom.* **2001**, *119*, 161–174.
133. Oulianov, D. A.; Tornov, I. V.; Dvornikov, A. S.; Rentzepis, P. M. *Proc. Natl. Acad. Sci. USA.* **2002**, *99*, 12556–12561.
134. Norman, D. *J. Synchrot. Radiat.* **2001**, *8*, 72–75.
135. Lamberti, C.; Prestipino, C.; Bonino, F.; Capello, L.; Bordiga, S.; Spoto, G.; Zecchina, A.; Moreno, S. D.; Cremaschi, B.; Garilli, M.; Marsella, A.; Carmello, D.; Vidotto, S.; Leofanti, G. *Angew. Chem.-Int. Edit.* **2002**, *41*, 2341–2344.
136. Ressler, T.; Wienold, J.; Jentoft, R. E.; Timpe, O.; Neisius, T. *Solid State Commun.* **2001**, *119*, 169–174.
137. Rodriguez, J. A.; Hanson, J. C.; Frenkel, A. I.; Kim, J. Y.; Perez, M. *J. Am. Chem. Soc.* **2002**, *124*, 346–354.
138. Yamaguchi, A.; Suzuki, A.; Shido, T.; Inada, Y.; Asakura, K.; Nomura, M.; Iwasawa, Y. *J. Phys. Chem. B* **2002**, *106*, 2415–2422.
139. Zhang, K.; Dong, J.; Auld, D. S. *Physica B* **1995**, *209*, 719–721.
140. Wasserman, S. R. *J. Physique* **1997**, *7*, 203–205.
141. Wasserman, S. R.; Allen, P. G.; Shuh, D. K.; Bucher, J. J.; Edelstein, N. M. *J. Synchrot. Radiat.* **1999**, *6*, 284–286.
142. Frenkel, A.; Kleifeld, O.; Wasserman, S. R.; Sagi, I. *J. Chem. Phys.* **2002**, *116*, 9449–9456.
143. Coulston, G. W.; Bare, S. R.; Kung, H.; Birkeland, K.; Bethke, G. K.; Harlow, R.; Nerron, N.; Lee, P. L. *Science* **1997**, *275*, 191–193.
144. Dent, A. J. *Top. Catal.* **2002**, *18*, 27–35.
145. Lutzenkirchen-Hecht, D.; Grundmann, S.; Frahm, R. *J. Synchrot. Radiat.* **2001**, *8*, 6–9.
146. Richwin, M.; Zaeper, R.; Lutzenkirchen-Hecht, D.; Frahm, R. *Rev. Sci. Instrum.* **2002**, *73*, 1668–1670.
147. Briois, V.; Moulin, C. C.; Verdaguer, M. *Actual Chim.* **2000**, 31–40.
148. Rehr, J. J.; Schattke, W.; de Abajo, F. J. G.; Muino, R. D.; Van Hove, M. A. *J. Electron Spectrosc. Relat. Phenom.* **2002**, *126*, 67–76.
149. Benfatto, M.; Della Longa, S. *J. Synchrot. Radiat.* **2001**, *8*, 1087–1094.
150. Sipr, O. *Phys. Rev. B* **2002**, *65*, art. no.-205115.
151. Kirby, J. A.; Goodin, D. B.; Wydrzynski, T.; Robertson, A. S.; Klein, M. P. *J. Am. Chem. Soc.* **1981**, *103*, 5537–5542.
152. Natoli, C. R. In *Springer Series in Chemical Physics*; Bianconi, A.; Incoccia, L., Stipcich, S., Eds.; Springer-Verlag: Berlin, 1983; Vol. 27.
153. Rehr, J. J.; Ankudinov, A. L. *J. Synchrot. Radiat.* **2001**, *8*, 61–65.
154. Shulman, R. G.; Yafet, Y.; Eisenberger, P.; Blumberg, W. E. *Proc. Natl. Acad. Sci. USA* **1976**, *73*, 1384–1388.
155. Hahn, J. E.; Scott, R. A.; Hodgson, K. O.; Doniach, S.; Desjardins, S. R.; Solomon, E. I. *Chem. Phys. Lett.* **1982**, *88*, 595–598.
156. Roe, A. L.; Schneider, D. J.; Mayer, R. J.; Pyrz, J. W.; Widom, J.; Que, L. *J. Am. Chem. Soc.* **1984**, *106*, 1676–1681.
157. Shadle, S. E.; Penner-Hahn, J. E.; Schugar, H. J.; Hedman, B.; Hodgson, K. O.; Solomon, E. I. *J. Am. Chem. Soc.* **1993**, *115*, 767–776.
158. Westre, T. E.; Kennepohl, P.; DeWitt, J. G.; Hedman, B.; Hodgson, K. O.; Solomon, E. I. *J. Am. Chem. Soc.* **1997**, *119*, 6297–6314.
159. George, G. N.; Cleland, W. E. J.; Enemark, J. H.; Smith, B. E.; Kipke, C. A.; Roberts, S. A.; Cramer, S. P. *J. Am. Chem. Soc.* **1990**, *112*, 2541–2548.
160. Cramer, S. P.; Ralston, C. Y.; Wang, H.; Bryant, C. *J. Electron Spectrosc. Relat. Phenom.* **1997**, *86*, 175–183.
161. George, S. J.; Lowery, M. D.; Solomon, E. I.; Cramer, S. P. *J. Am. Chem. Soc.* **1993**, *115*, 2968–2969.
162. Steinberger, I. T.; Teodorescu, C. M.; Gravel, D.; Flesch, R.; Wassermann, B.; Reichardt, G.; Hutchings, C. W.; Hitchcock, A. P.; Ruhl, E. *Phys. Rev. B* **1999**, *60*, 3995–4004.
163. Federmann, F.; Bjorneholm, O.; Beutler, A.; Moller, T. *Phys. Rev. Lett.* **1994**, *73*, 1549–1552.
164. Colpas, G. J.; Maroney, M. J.; Bagyinka, C.; Kumar, M.; Willis, W. S.; Suib, S. L.; Baidya, N.; Mascharak, P. K. *Inorg. Chem.* **1991**, *30*, 920–928.
165. Smith, T. A.; Penner-Hahn, J. E.; Berding, M. A.; Doniach, S.; Hodgson, K. O. *J. Am. Chem. Soc.* **1985**, *107*, 5945–5955.

166. Kau, L. S.; Spira-Solomon, D. J.; Penner-Hahn, J. E.; Hodgson, K. O.; Solomon, E. I. *J. Am. Chem. Soc.* **1987**, *109*, 6433–6442.
167. Pickering, I. J.; George, G. N. *Inorg. Chem.* **1995**, *34*, 3142–3152.
168. Shadle, S. E.; Hedman, B.; Hodgson, K. O.; Solomon, E. I. *J. Am. Chem. Soc.* **1995**, *117*, 2259–2272.
169. Glaser, T.; Hedman, B.; Hodgson, K. O.; Solomon, E. I. *Acc. Chem. Res.* **2000**, *33*, 859–868.
170. Neese, F.; Hedman, B.; Hodgson, K. O.; Solomon, E. I. *Inorg. Chem.* **1999**, *38*, 4854–4860.
171. Bianconi, A.; Li, C.; Campanella, F.; Della Longa, S.; Pettiti, I.; Pompa, M.; Turtu, S.; Udron, D. *Phys. Rev. B: Condens. Matter* **1991**, *44*, 4560–4569.
172. Li, C.; Pompa, M.; Castellano, A. C.; Della Longa, S.; Bianconi, A. *Physica C (Amsterdam)* **1991**, *175*, 369–80.
173. Yokoyama, T.; Kosugi, N.; Kuroda, H. *Chem. Phys.* **1986**, *103*, 101–109.
174. Kosugi, N.; Yokoyama, T.; Kuroda, H. *Springer Proc. Phys.* **1984**, *2*, 55–57.
175. Kosugi, N.; Yokoyama, T.; Asakura, K.; Kuroda, H. *Chem. Phys.* **1984**, *91*, 249–256.
176. Sipr, O.; Simunek, A. *J. Phys.-Condes. Matter* **2001**, *13*, 8519–8525.
177. Solomon, E. I.; Randall, D. W.; Glaser, T. *Coord. Chem. Rev.* **2000**, *200*, 595–632.
178. Elleaume, P. *J. Synchrot. Radiat.* **1994**, *1*, 19–26.
179. Elleaume, P.; Chavanne, J.; Marechal, X.; Goulon, J.; Braicovich, L.; Malgrange, C.; Emerich, H.; Marot, G.; Susini, J. *Nucl. Instrum. Methods Phys. Res. Sect. A-Accel. Spectrom. Dect. Assoc. Equip.* **1991**, *308*, 382–389.
180. Varga, L.; Giles, C.; Zheng, Y. L.; Pizzini, S.; de Bergevin, F.; Fontaine, A.; Malgrange, C. *J. Synchrot. Radiat.* **1999**, *6*, 1125–1132.
181. Hirano, K.; Ishikawa, T.; Kikuta, S. *Nucl. Instrum. Methods Phys. Res. Sect. A-Accel. Spectrom. Dect. Assoc. Equip.* **1993**, *336*, 343–353.
182. Hahn, J. E.; Hodgson, K. O. *ACS Symposium Series* 1983, *211*, 431–444.
183. de Groot, F. M. F. *J. Electron Spectrosc. Relat. Phenom.* **1994**, *67*, 529–622.
184. Beni, G.; Platzman, P. M. *Phys. Rev. B* **1976**, *14*, 1514–1518.
185. Pellicer-Porres, J.; Segura, A.; Munoz, V.; San Miguel, A. *Phys. Rev. B: Condens. Matter Mater. Phys.* **2000**, *61*, 125–131.
186. Mustre de Leon, J.; Conradson, S. D.; Batistic, I.; Bishop, A. R.; Raistrick, I. D.; Aronson, M. C.; Garzon, F. H. *Phys. Rev. B: Condens. Matter* **1992**, *45*, 2447–2457.
187. Scott, R. A.; Hahn, J. E.; Doniach, S.; Freeman, H. C.; Hodgson, K. O. *J. Am. Chem. Soc.* **1982**, *104*, 5364–5369.
188. Schlegel, M. L.; Manceau, A.; Chateigner, D.; Charlet, L. *J. Colloid Interface Sci.* **1999**, *215*, 140–158.
189. Oyanagi, H.; Sugi, M.; Kuroda, S.; Iizima, S.; Ishiguro, T.; Matsushita, T. *Thin Solid Films* **1985**, *133*, 181–188.
190. Dau, H.; Andrews, J. C.; Roelofs, T. A.; Latimer, M. J.; Liang, W. C.; Yachandra, V. K.; Sauer, K.; Klein, M. P. *Biochemistry* **1995**, *34*, 5274–5287.
191. Schiller, H.; Dittmer, J.; Iuzzolino, L.; Dorner, W.; Meyer-Klaucke, W.; Sole, V. A.; Nolting, H. F.; Dau, H. *Biochemistry* **1998**, *37*, 7340–7350.
192. Edwards, A. M.; Zhang, K.; Nordgren, C. E.; Blasie, J. K. *Biophys. J.* **2000**, *79*, 3105–3117.
193. Uozumi, T.; Okada, K.; Kotani, A.; Durmeyer, O.; Kappler, J. P.; Beaurepaire, E.; Parlebas, J. C. *Europhys. Lett.* **1992**, *18*, 85–90.
194. Cabaret, D.; Joly, Y.; Renevier, H.; Natoli, C. R. *J. Synchrotron Radiat.* **1999**, *6*, 258–260.
195. Kosugi, N.; Yokoyama, T.; Kuroda, H. *Chem. Phys.* **1986**, *104*, 449–453.
196. van Elp, J.; Searle, B. G. *J. Electron Spectrosc. Relat. Phenom.* **1997**, *86*, 93–106.
197. Chakarian, V.; Idzerda, Y. U.; Meigs, G.; Chen, C. T. *IEEE Trans. Magn.* **1995**, *31*, 3307–3312.
198. Schuetz, G.; Knuelle, M.; Ebert, H. *Phys. Scr., T* **1993**, *T49A*, 302–306.
199. van Elp, J.; George, S. J.; Chen, J.; Peng, G.; Chen, C. T.; Tjeng, L. H.; Meigs, G.; Lin, H. J.; Zhou, Z. H.; Adams, M. W. W.; Searle, B. G.; Cramer, S. P. *Proc. Natl. Acad. Sci. USA* **1993**, *90*, 9664–9667.
200. Popescu, V.; Ebert, H.; Ahlers, D. *J. Magn. Magn. Mater.* **1999**, *191*, 368–372.
201. Schutz, G.; Ahlers, D. *J. Physique* **1997**, *7*, 59–65.
202. Isnard, O.; Miraglia, S.; Fruchart, D.; Giorgetti, C.; Dartyge, E.; Krill, G. *J. Phys.-Condes. Matter* **1996**, *8*, 2437–2446.
203. Alagna, L.; Prosperi, T.; Turchini, S.; Goulon, J.; Rogalev, A.; Goulon-Ginet, C.; Natoli, C. R.; Peacock, R. D.; Stewart, B. *Phys. Rev. Lett.* **1998**, *80*, 4799–4802.
204. Stewart, B.; Peacock, R. D.; Alagna, L.; Prosperi, T.; Turchini, S.; Goulon, J.; Rogalev, A.; Goulon-Ginet, C. *J. Am. Chem. Soc.* **1999**, *121*, 10233–10234.
205. Natoli, C. R.; Brouder, C.; Sainctavit, P.; Goulon, J.; Goulon-Ginet, C.; Rogalev, A. *Eur. Phys. J. B* **1998**, *4*, 1–11.
206. Brouder, C.; Natoli, C. R.; Sainctavit, P.; Goulon, J.; Goulon-Ginet, C.; Rogalev, A. *J. Synchrot. Radiat.* **1999**, *6*, 261–263.
207. Goulon, J.; Goulon-Ginet, C.; Rogalev, A.; Benayoun, G.; Brouder, C.; Natoli, C. R. *J. Synchrotron Radiat.* **2000**, *7*, 182–188.
208. de Groot, F. *Chem. Rev.* **2001**, *101*, 1779–1808.
209. Hamalainen, K.; Siddons, D. P.; Hastings, J. B.; Berman, L. E. *Phys. Rev. Lett* **1991**, *67*, 2850–2853.
210. Glatzel, P.; Jacquamet, L.; Bergmann, U.; de Groot, F. M. F.; Cramer, S. P. *Inorg. Chem.* **2002**, *41*, 3121–3127.
211. de Groot, F. M. F. *Top. Catal.* **2000**, *10*, 179–186.
212. Hamalainen, K.; Kao, C. C.; Hastings, J. B.; Siddons, D. P.; Berman, L. E.; Stojanoff, V.; Cramer, S. P. *Phys. Rev. B: Condens. Matter* **1992**, *46*, 14274–14277.
213. Bertsch, P. M.; Hunter, D. B. *Chem. Rev.* **2001**, *101*, 1809–1842.
214. Sutton, S. R.; Rivers, M. L.; Bajt, S.; Jones, K.; Smith, J. V. *Nucl. Instrum. Methods Phys. Res., Sect. A* **1994**, *347*, 412–416.
215. Sutton, R. S.; Bajt, S.; Delaney, J.; Schulze, D.; Tokunaga, T. *Rev. Sci. Instrum* **1995**, *66*, 1464–1467.
216. Kirz, J.; Jacobsen, C.; Howells, M. *Q. Rev. Biophys.* **1995**, *28*, 33–130.
217. Dhez, P.; Chevallier, P.; Lucatorto, T. B.; Tarrio, C. *Rev. Sci. Instrum.* **1999**, *70*, 1907–1920.
218. Snigirev, A.; Kohn, V.; Snigireva, I.; Lengeler, B. *Nature* **1996**, *384*, 49–51.
219. Anderson, A. J.; Jayanetti, S.; Mayanovic, R. A.; Bassett, W. A.; Chou, I. M. *Am. Miner.* **2002**, *87*, 262–268.

220. Cabri, L. J.; Newville, M.; Gordon, R. A.; Crozier, E. D.; Sutton, S. R.; McMahon, G.; Jiang, D. T. *Can. Mineral.* **2000**, *38*, 1265–1281.
221. Bertsch, P. M.; Hunter, D. B.; Sutton, S. R.; Bajt, S.; Rivers, M. L. *Environ. Sci. Technol.* **1994**, *28*, 980–984.
222. Hunter, D. B.; Bertsch, P. M.; Kemner, K. M.; Clark, S. B. *J. Physique* **1997**, *7*, 767–771.